Role of particle size on the cohesive behavior of limestone powders at high temperature

M. J. Espin[a], F. J. Duran-Olivencia[b], J. M. Valverde[b,*]

[a]*Departamento de Fisica Aplicada II, Universidad de Sevilla. Avenida Reina Mercedes s/n, 41012 Sevilla, Spain*
[b]*Facultad de Fisica, Universidad de Sevilla. Avenida Reina Mercedes s/n, 41012 Sevilla, Spain*

Abstract

Thermal Energy Storage (TES) using granular solids is gaining momentum in the last years. With no degradation up to very high temperatures and very low price the use of some granular materials such as sand or SiC would be feasible for storing sensible heat at large scale. A further step beyond TES is thermochemical energy storage (TCES) wherein the granular solids undergo a highly endothermic reaction at high temperature. Energy can be in this way more efficiently stored in the long term and released on demand by means of the reverse exothermic reaction. The Calcium Looping process, based on the calcination/carbonation of $CaCO_3$, is being actively investigated for this purpose. However, a caveat of using granular solids for energy storage is the possible increase of interparticle adhesive forces with temperature which would severely hamper the flowability of the solids in the

---

[*]Corresponding author
Email addresses: `mjespin@us.es` (M. J. Espin), `fjduroli@us.es` (F. J. Duran-Olivencia), `jmillan@us.es` (J. M. Valverde)

process. The cohesiveness of granular materials is essentially determined by particle size. In this paper we investigate the dependence of the tensile yield strength and compressibility of $CaCO_3$ powders on temperature and consolidation stress using samples of narrow particle size distribution in the relevant range between ~ 30 and $\sim 80\,\mu$m particle size and temperatures up to 500°C. Our experimental results show that powder cohesiveness is greatly increased with temperature especially in the case of the finest powders whose tensile yield strength can be increased by up 2 orders of magnitude. The increase of cohesiveness with temperature is further enhanced with a previously applied consolidation stress, which is particularly relevant for applications wherein large amounts of solids are to be stored at high temperature. Experimental data are consistent with the predictions by a contact mechanics model assuming that the solids deform plastically at interparticle contacts. A main conclusion from our work is that some mechanical properties of the solids, specially the mechanical hardness, and how they change with temperature, play a critical role on the flowability of the solids as affected by an increase of temperature.

1. Introduction

The commercial expansion of renewable energy at large scale is urgently needed for mitigating global warming. Renewable energy sources have the potential to supply clean, affordable and sufficient power to replace fossil fuels in the medium term while simultaneously satisfy the ever growing energy demands [1]. However, increasing the degree of penetration of the main renewable energies, such as solar and wind, in the power grid will not be possible until large-scale energy storage is incorporated to power generation plants to cope with the intermittent nature of these clean energy resources [2–5].

Thermal energy storage (TES) in sensible form has already reached a commercial stage in concentrating solar power (CSP) plants with central tower technology enabling electricity generation when sunlight is not available or during low radiation hours [6–9]. These CSP plants with energy storage basically consist of a set of heliostats orientated to concentrate solar radiation in a solar receiver at the top of a tower where a heat transfer fluid can be heated to temperatures up to 1000°C [10–12].

Sensible heat storage (SHS) fluids or solids store/release sensible heat during the process of heating/cooling. Their main working requirements are an extended temperature range to avoid phase change and degradation, high thermal conductivity for efficient heat transfer, low viscosity (for SHS fluids) to avoid large pressure drops during pumping, high heat capacity, safety, non-corrosiveness and low cost [13–15]. Commonly used SHS materials in

commercial CSP plants are water/steam and molten salts. Water/steam [16] seems to be the best option available because of its low cost, high specific heat capacity, wide availability and chemical stability. A limited temperature range (≤ 100°C at atmospheric pressure) is yet an important drawback for its large-scale application. This issue may be overcome by increasing steam pressure (even up to 35 bar for industrial purposes) which adds however excessive costs [13]. Nowadays, most commercial CSP plants with integrated energy storage use solar salts (usually a binary sodium-potassium nitrate compound in a molten state [17]) as SHS fluid [11, 18]. Main advantages of these solar salts are their high heat capacity and relative low cost. However, molten salts degrade at temperatures beyond ~ 560°C and solidify below 200°C which limits their working temperature range [19, 20]. Corrosiveness of solar salts poses also a main inconvenient as it raises operation and maintenance costs [21, 22].

Solid materials such as sand, SiC, concrete or fire bricks [6, 23] are being investigated as good alternatives to molten salts [6, 24–27]. SHS solids are not corrosive nor environmentally unfriendly and may operate at much higher temperatures than molten salts without degradation. Nevertheless their heat capacity is appreciably lower which makes necessary the use of very large units to store sufficient energy [28].

Latent heat storage (LHS) relies on the heat stored/released when materials undergo a phase transition [28]. Phase change materials (PCMs) for TES applications should have an adequate phase transition temperature,

4

high thermal conductivity, long-term chemical stability, safety, low cost and, overall, their volume change during the phase transition should be as small as possible to avoid storage problems [29]. Phase changes yielding the highest latent heat are solid-gas and liquid-gas transitions but they involve large volume changes which causes excessive complexity and economic cost [30]. Thus, most industrial efforts have been focused on PCMs that undergo solid-liquid phase changes in the typical range of temperatures taking place in CSP plants [30]. These PCMs suffer a small volume change during the phase transition but the associated latent heat is low [13, 29, 31]. Paraffin, fatty acids and salt hydrates are some of the most widespread used PCMs [32]. For the same temperature range, LHS systems have larger heat storage capacity than SHS materials and heat is stored in a nearly isothermal process. Degradation by dehydration, chemical decomposition and maintenance costs are the principal disadvantages of PCMs with respect to fluids and solids used in SHS systems [29, 33]. In addition, most PCMS are operated in low temperature ranges (up to $\sim 90°$C) which makes them suitable for residential applications [28, 33] but not for CSP with tower technology.

The less mature but highly promising technology for heat storage in CSP plants with tower technology consists of thermochemical energy storage (TCES) [34–37]. TCES systems are based on the storage/release of heat by means of reversible chemical reactions with high enthalpy [38–40]. The high temperatures achievable in the solar receiver of CSP plants can supply the required heat to drive highly endothermic chemical reactions. The

by-products of the endothermic reaction are stored separately and brought together on demand. Then, at suitable reaction conditions, the previously used heat is released in the reverse exothermic reaction. TCES systems can store energy with a theoretically high density and are suitable to work at higher temperatures compared to SHS and LHS systems [33, 41–43]. A main potential benefit of TCES is the possibility of long-term storage, including long-distance transport of the reactants (and, hence, the heat stored), at ambient temperature without significant losses. Till the date, the majority of works at lab- and pilot-scale on TCES have been focused on redox-based systems [44–46]. Another interesting option to integrate TCES in CSP plants is the Calcium-Looping process (CaL) based on the reversible calcination/carbonation reaction of $CaCO_3/CaO$ [47–51]

$$CaCO_{3(s)} \rightleftarrows CaO_{(s)} + CO_{2(g)}; \ \Delta Hr^0 = 178kJ/mol. \tag{1}$$

The $CaCO_3/CaO$ system presents several advantages as compared to other TCES systems. These compounds are non-toxic, non-corrosive, environmentally friendly, abundant, cheap and naturally occurring as raw minerals [38, 47]. The reversible calcination/carbonation reaction has been thoroughly investigated and technically developed at large pilot-scale $(1 - 2\,\mathrm{MWth})$ to capture CO_2 in fossil fuel power plants [52–57] and cement and lime manufactures [58–62] with successful results [56, 63–66].

Lab-scale experiments and simulations using limestone powder (almost

pure $CaCO_3$) demonstrate a number of advantages of the CaL process to store energy in chemical form [11, 34–37]. Mainly, high energy storage densities can be potentially achieved (theoretically up to $3.26\,\mathrm{GJm^{-3}}$ vs. $0.5\,\mathrm{GJm^{-3}}$ for molten salts [47, 67–70]). These materials present also a high thermal conductivity (around $1.5\,\mathrm{Wm^{-1}K^{-1}}$, which is about three times higher than solar salts [71]).

The integration of the CaL process into CSP plants with central tower technology for energy storage is being currently tested at the small pilot scale in Europe within the SOCRATCES project [72] and in USA (DOE) under the APOLLO [73] and ELEMENTS programs [74]. Direct solar irradiation provided by an heliostats field would be used to calcine the $CaCO_3$ particles in a solar calciner reactor [51]. In the SOCRATCES project Sensible heat of the subsequent products of the calcination reaction (CaO and CO_2) are recovered by heat exchangers before storing them separately at ambient temperature [51]. Alternatively, the solids can be stored at high temperature for short-term use to increase the overall efficiency [69]. When required, the reaction byproducts are recirculated and mixed in a carbonator reactor where the reversible carbonation reaction takes place at high temperature and high CO_2 partial pressure. The released heat from this exothermic reaction is transported to a gas turbine by the excess CO_2 over the stoichiometric ratio not intervening in the carbonation reaction to produce electricity by means of a Joule–Brayton cycle [47]. Thus, tailoring the calcination/carbonation reaction of $CaCO_3/CaO$ would enable electric power generation on demand.

The CaL process would be likely carried out in circulating fluidized bed reactors, where the high gas-solid contact efficiency would enhance the performance of the calcination/carbonation reactions [24, 47, 50, 57, 72]. Moreover, the mixture of solid particles and gas in fluidized beds promotes temperature uniformity and heat transfer between reagents [75]. However, a key property that may compromise the efficiency of fluidized bed reactors as well as the transport of particles within the system is the cohesive behavior of the granular material which depends critically on particle size [76]. Recent studies on the role of particle size on the CaL process have been focused on thermogravimetric tests targeting the multicycle reactivity of limestone derived CaO when cycled under calcination/carbonation conditions for CO_2 capture [77–80] and for TCES [81]. To the best of authors' knowledge, the role of particle size on the flowability of $CaCO_3$/CaO powders at high temperatures remains unexplored.

As particle size is decreased, the gas-solid contact efficiency is increased but also the cohesiveness of the powder [82]. Fine particles in cohesive powders (belonging to the Geldart C type [83]) form large agglomerates impermeable to the gas flow. As a consequence, stable gas channels are usually developed in the bulk of the powder through which most of the gas flow bypasses the bed, which hinders the gas-solid contact efficiency in fluidized beds. Moreover, the flow of cohesive powders becomes severely impaired as stable arches are prone to be developed and jamming is promoted [84]. Typically, powder cohesiveness becomes significant when particle size is de-

creased below $\sim 50\,\mu$m [82]. Blockage of stand-pipes and discontinuous flow are prone to occur in cement plants for Ca-based powders of particle size below $\sim 30\,\mu$m [85]. Moreover, poor flowability is usually enhanced after powders are stored for a long period of time, which may promote interparticle adhesive forces [86, 87]. Since powder cohesiveness may be also enhanced as the temperature increases, free flowing powders at ambient temperature could turn into cohesive at high temperatures [88]. Thus, the influence of particle size and temperature on powder flowability must be taken under consideration for solids transport and storage [89].

Knowing how temperature and particle size may affect limestone flowability may help understand the governing mechanism behind the increase of powder cohesiveness with temperature. This basic knowledge would be useful for applications based on the CaL process such as CO_2 capture and energy storage in CSP plants. Other applications currently under research and development that might benefit from this fundamental research are solar irradiated rotary kilns [90] and sensible heat storage where other solid granular materials must flow and be transported at high temperatures [28].

In this work, we have investigated the cohesiveness of a set of $CaCO_3$ powders as affected by particle size at high temperatures and previously subjected to a range of relatively low consolidation stresses between $\sim 100\,$Pa and a few kPa which are relevant to powder flow. The average particle size of the tested $CaCO_3$ powders ranges between ~ 30 and $\sim 80\,\mu$m which belongs to the range of interest for industrial purposes in the integration of the CaL

process in CSP plants for TCES [72]. As inferred from thermogravimetric studies, CaL conditions used in this application hinder CaO reactivity due to pore plugging when limestone particle size is increased above $\sim 50\,\mu$m. The use of fine limestone powders to avoid this inconvenient as regards multicycle reactivity requires on the other hand assessing how cohesiveness is enhanced with temperature. This is the main goal of the present study.

2. Materials and experimental setup

2.1. Materials

The granular materials used in this work were purchased from KSL staubtechnik gmbh and consisted of $CaCO_3$ powder samples (particle density $\rho_{\mathrm{p}} = 2700\,$kg/m^3) of four different well-defined volume average particle diameters d_{p}. Commercial names are [91]: Eskal30 ($d_{\mathrm{p}} = 32.29 \pm 0.97\,\mu$m), Eskal45 ($d_{\mathrm{p}} = 42.5 \pm 0.8\,\mu$m), Eskal60 ($d_{\mathrm{p}} = 59.3 \pm 0.8\,\mu$m) and Eskal80 ($d_{\mathrm{p}} = 88.2 \pm 0.7\,\mu$m). These samples are commercially available and have been used in a previous work by Shi et al. [92] to analyze the effect of particle size on powder flowability at ambient temperature by employing a number of commercial shear testers. As can be seen from SEM images in Figure 1, $CaCO_3$ particles are irregularly shaped and size dispersion is small. Measurements of the particle size distributions (Figure 2) confirm that these particles exhibit a low level of polydispersion which makes them suitable for investigating the effect of particle size on powder cohesiveness without the influence of other confounding factors.

10

Mechanical properties measured at room temperature of $CaCO_3$ particles reported in the literature such as Young's modulus, mechanical hardness, Poisson ratio and surface energy (relevant to powder cohesiveness [82]) are summarized in Table 1. As may be seen, the values of these properties belong to a wide range which is partly due to the use of diverse experimental procedures. For instance, the determination of mechanical hardness is quite sensitive to the type of microindenter (elongated or symmetric) employed [93–95]. In the discussion of our experimental results (section 3), we will use the central values in the ranges reported in the literature for these properties: Young's modulus $E \approx 5.66 \times 10^{10}$ Pa, Poisson ratio $\nu \approx 0.28$, surface energy $\gamma \approx 0.33$ J/m^2 and mechanical hardness $H \approx 2.93 \times 10^9$ Pa.

2.2. Experimental setup

Figure 3 depicts a schematic view of the self-made equipment used in our work to measure the tensile yield strength of cohesive powders at high temperature as a function of the previously applied consolidation stress. The device is based on the original Sevilla Powder Tester (SPT) characterization device which was engineered by our research group and has been employed in many previous works, and in diverse research centers, to test different types of powders [82, 96–101].

Extensive descriptions on the functioning of the SPT are available elsewhere for the interested reader [98, 102]. Only a brief review will be given here just to highlight the modifications implemented to carry out the tests

at high temperatures. The powder sample is held in a vertically oriented cylindrical quartz vessel (4.5 cm inner diameter) where it rests over a porous ceramic plate which serves as gas distributor. The inlet air flow is beforehand passed across a set of filters and a refrigerated air dryer (model SMC IDFA3E) to remove any pollutants and humidity (which is known to significantly affect powder cohesiveness [103]). The filtered and dried gas flow is pumped in the bed by means of a digital mass flow controller (Omega model FMA-2606A, 2000 sccm). The pressure drop of the gas across the powder bed is measured using a differential pressure transducer (MKS model 220CD, 10 Torr full scale). Four electrical valves (SMC) are employed to set the direction of the gas flow across the powder bed. The gas flows upward to put the powder bed under tension if valves 1 and 2 are open (3 and 4 closed) whereas the gas flows downward to compress the bed when valves 3 and 4 are open (1 and 2 closed). The sound generation system on top of the bed consists of an electric signal generator producing an electric sine wave of a fixed frequency that is sent to an amplifier. The amplified signal excites a woofer loudspeaker to generate a low frequency sound wave. A PVC pipe is used to guide the sound wave to the quartz vessel. To avoid the gas exchange between the vessel and the sound system a silicone elastic membrane (with good sound transmission properties) is placed inside the sound guide. The quartz reactor is heated by an electric furnace monitored by a PID temperature controller (Eurotherm 3216). All these components are connected to a computer by means of a data acquisition board. The whole measuring

procedure is automated to ensure reproducibility of the experimental results.

Experimental tests begin with the initialization of the sample ($m_\mathrm{p} = 60\,\mathrm{g}$) by imposing an upward large enough gas flow rate to drive the powder bed into the freely bubbling regime. Simultaneously, an acoustic field of low frequency ($130\,\mathrm{Hz}$) and high intensity ($150\,\mathrm{dB}$) is applied for 5 seconds to help the gas flow break up any possible channels or plugs likely developed in the case of highly cohesive powders [104]. The powder bed is allowed to bubble for 30 seconds, which is a sufficiently long period of time to erase the powder memory of previous processes [105]. Then, the gas flow rate is suddenly ceased and the particles are let to settle for 30 seconds into a reproducible state. This important initialization procedure sets repeatable starting condition for testing the powder. Thereafter, the heating stage begins. Once the internal temperature in the furnace reaches the target temperature (in a range between 25 and 500°C in the tests hereafter reported), a thermal stabilization time for one hour is set to assure that the whole mass of powder achieves the selected temperature. The next stage consists of consolidating the sample by the imposition of an increasing downward directed gas flow rate. The compressing gas imposes a homogeneously distributed pressure over the bed pressing it against the ceramic distributor plate. Thus, the consolidation stress at the bottom of the bed is given by the gas pressure drop across it plus the powder weight per unit area $\sigma_\mathrm{c} = \Delta p + W$. Once the target consolidation stress is reached, the corresponding downward flow rate is kept fixed for a consolidation time of 10 seconds and then it is pro-

13

gressively reduced to zero (as will be shown ahead the effect of varying the consolidation time has been also tested in our work). In the last stage of the test, an upward gas flow is increased gradually to break the powder bed under tension which gives a measure of the powder tensile yield strength as a function of the previously applied consolidation stress.

3. Results

3.1. Fluidization curves as affected by consolidation stress, particle size and temperature

Figure 4 shows experimental curves of the gas pressure drop across the powder bed Δp (made non-dimensional with the powder's weight per unit area W) as a function of the gas (mass) flow rate q_{m} for samples of $CaCO_3$ powders of different particle size d_{p} at room temperature. Let us describe first the evolution of the powder bed as reflected by these fluidization curves. As q_{m} is slowly increased from zero, the structure of the bed remains initially unperturbed in a solid-like state determined by the previously applied consolidation stress. Under these conditions, Δp is due to the frictional resistance across the bed and increases linearly with q_{m}. At the low Reynolds numbers involved in our tests, this linear behavior is described by the well-known Carman-Kozeny law [106] which can be expressed in terms of the slope $s = \Delta p / q_{\mathrm{m}}$ as follows:

$$s = \frac{\Delta p}{q_{\mathrm{m}}} = \frac{E}{\Psi_{\mathrm{p}}^2 d_{\mathrm{p}}^2} \frac{\eta}{\rho} \frac{h}{S} \frac{\phi^2}{(1-\phi)^3}. \tag{2}$$

14

where E is the Ergun's empirical constant ranging from 150 to 180 [107]; Ψ_p is the sphericity of the particle (the ratio of the surface area of a sphere with the same volume as the actual particle to the surface area of the particle); η is the dynamic viscosity of the gas; ρ denotes the density of the gas; h and S are the height and cross sectional area of the bed, respectively; and ϕ is the particle volume fraction.

At the minimum fluidization gas flow rate q_{mf}, Δp equals W. In this point a free flowing noncohesive powder would become fluidized in a liquid-like state. However, for cohesive powders, interparticle adhesive forces prevent the bed from fluidization. Further increase of q_m puts the bed under tension while the gas pressure drop continuous to increase linearly till interparticle adhesive forces are overcome. At this critical value of q_m, the powder bed fractures and Δp falls abruptly. Visual observations show that the first fracture occurs on a surface, within the powder, close to the bottom of the bed where the tensile stress is maximum as theoretically predicted [98, 102, 108]. The observed overshoot of the gas pressure drop over the powder weight per unit area gives therefore a value of the powder tensile yield strength $\sigma_t = \Delta p_{max} - W$. In all tests carried out in this work, the height of the bed was always smaller than its diameter (shallow beds) therefore wall stresses can be neglected [109]. Further increase of q_m causes the upward propagation of the fracture to the rest of the powder bed giving rise to a state of heterogeneous fluidization while the value of Δp fluctuates around W.

Figure 4 also illustrates the dependence of particle size on the fluidization

behavior of the powder. At a given temperature and consolidation stress, the tensile yield strength σ_t is increased as particle size is decreased. Interestingly, the slope s also depends markedly on d_p. As particle size increases from $d_p \sim 30\,\mu$m to $d_p \sim 60\,\mu$m, the slope s is progressively diminished. The reduction of s becomes more pronounced for powder beds of larger particle size ($d_p \sim 80\,\mu$m). As will be seen below this dependence of the slope s on particle size is a consequence of the variation of the particle volume fraction of the settled powders with particle size.

Gas pressure drop measurements also serve to investigate the role of temperature T on the fluidization behavior of the powder. Figure 5 exemplifies data obtained of Δp (normalized by the powder's weight per unit area W) vs. the gas flow rate for the $CaCO_3$ powder of particle size $d_p \sim 60\,\mu$m previously subjected to a consolidation stress $\sigma_c = 1500\,$Pa and for tests carried out at different temperatures. As may be observed in Figure 5, the tensile yield strength of the powder is appreciably increased as the temperature is increased. The initial slope s is also clearly dependent on T. Thus, the values of s increase significantly when T raises from 25 to 300°C. However, at temperatures beyond 300°C, the enhancement of s with T becomes less marked.

Figure 6 illustrates the effect of the previously imposed consolidation stress on the fluidization behavior of the tested $CaCO_3$ powders. The values of σ_t increase considerably as the powder is subjected to increasing values of σ_c. However, the influence of σ_c on the initial slope s is less noticeable as

compared to the effects of d_p and T.

At this point, it is worth wondering whether these results are also dependent on the period of time during which the powder beds were subjected to a given consolidation stress. This effect is well-known in powder technology (caking) and consists of the enhancement of powder cohesiveness of loaded powders with time due to the viscoplastic nature of interparticle contacts for some materials [82, 87, 110]. Caking is particularly relevant when powders are allowed to settle for relatively long periods of time between successive uses, as might occur for $CaCO_3$ powders in TCES systems or for CO_2 capture where large masses of limestone would be stored in silos [47, 70, 72, 111]. The modified STP used in this work is also able to measure σ_t as a function of the consolidation time τ (time of application of σ_c). Figure 7 shows data on the average values of σ_t measured for $CaCO_3$ samples ($d_p \sim 45\,\mu m$) subjected to a consolidated stress σ_c equal to their own weight per unit area W and for increasing periods of time. Consolidation time ranges between just 10 seconds to one hour. The experiments were performed at different temperatures. As clearly observed, within the accuracy of our measurements, σ_t does not change appreciably with the consolidation time regardless of temperature, which indicates that caking in $CaCO_3$ powders is not relevant even at the high temperatures and for the time lags employed in our work. Data shown in Figure 7 serve also to demonstrate the reproducibility of the results obtained in our experimental tests.

3.2. Effect of temperature, particle size and consolidation stress on the tensile yield strength

Figure 8 shows data of the measured tensile yield strength of $CaCO_3$ powders as a function of σ_c, T, and d_p. First, we will analyze the effect of σ_c for powders with a given particle size and tests carried out at a fixed temperature. As expected from Figure 6, increasing consolidation stresses lead to higher tensile yield strengths. In agreement with previous studies carried out at ambient temperature on diverse types of fine powders [68, 100], the rate of increase of σ_t with σ_c follows a sublinear trend, $\sigma_t = a\sigma_c^b$ with $b \lessapprox 1$ (Table 2).

At a given particle size d_p, the tensile yield strength of the powders is clearly increased when T raises from 25 to 500°C as was inferred from the fluidization curves (Figure 5). This effect is appreciable in the whole range of temperatures tested in our work but becomes more marked for $T \geq 300$°C. It must be also underlined that the increase of σ_t with T is influenced by the previously imposed consolidation stress. As σ_c increases, the effect of T becomes remarkable giving rise to an increase in σ_t of up to two orders of magnitude for the highest consolidation stress tested ($\sigma_c \approx 2000$ Pa) when the temperature is increased from 25°C to 500°C. This cross effect of T and σ_c can be also observed in the exponent of the power law $\sigma_t = a\sigma_c^b$. As the temperature of the powder bed becomes higher, b gradually increases from ~ 0.3 to ~ 0.9 (Table 2).

Finally, we will describe the role of d_p on the tensile yield strength as

affected by temperature and the consolidation stress. At a given temperature, the tensile yield strength of the powder increases with the consolidation stress in a less pronounced manner the larger the particle size (as was inferred from Figure 4). The decrease of σ_t with d_p is not gradual yet. When d_p is decreased from $\sim 80\,\mu$m to $\sim 45\,\mu$m, σ_t increases smoothly but from $\sim 45\,\mu$m to $\sim 30\,\mu$m the enhancement of σ_t is neatly more marked. The influence of T on σ_t is also affected by particle size. There is an appreciable increase in the tensile yield strength for temperatures as low as $\sim 100°$C when particle size is small $(d_p \sim 30\,\mu$m$)$. However, higher temperatures are required to cause a significant enhancement of σ_t as particle size increases. For instance, for $d_p \sim 45\,\mu$m, there is no relevant effect of T on the tensile yield strength until the temperature is increased over 200°C whereas this threshold is increased to 300°C in the case of $d_p \sim 60\,\mu$m and $d_p \sim 80\,\mu$m.

As a preliminary conclusion, our results demonstrate that the particle size of $CaCO_3$ powders employed in industrial applications determines critically the flow behavior of these powders as depending on temperature. Thus, a decrease of d_p below $\sim 80\,\mu$m yields a significant enhancement of powder cohesiveness as the temperature is increased over $\sim 100°$C at relatively small consolidation stresses relevant to powder flow. Since the storage of $CaCO_3$ powders in industrial-scale plants may lead to consolidation stresses well above 1 kPa at temperatures higher than 300°C [72], it is a foregone conclusion that the flowability of $CaCO_3$ powders will be severely hindered at the high temperatures typical of the CaL process.

3.3. Influence of temperature, particle size and consolidation stress on the micro-structure of $CaCO_3$ powder beds

Information on the micro-structure of the tested $CaCO_3$ powders can be inferred from the particle volume fraction after the powder has been consolidated under a stress σ_c. Using Equation 2, ϕ can be calculated from the initial slope $s = \Delta p / q_m$ (Figure 4). All the parameters involved in this equation are known with the exception of the ratio E/ψ_p^2, which depends on particle shape. To estimate it, we will use experimental data for samples of $d_p \sim 30\,\mu m$ which were initially subjected to a consolidation stresses σ_c in the range between W and $\sim 5\,kPa$ at room temperature. In these tests, the particle volume fraction could be obtained from direct measurements of the height h of the consolidated powder bed ($\phi = m_p/(\rho_p h S)$) by means of an ultrasonic sensor mounted on top of the bed using the original setup of the SPT [98, 102] (at high temperatures the use of the ultrasonic sensor was not possible due to technical limitations). The initial slope $s = \Delta p / q_m$ was also obtained in these tests at ambient temperature from the fluidization curve. Figure 9 shows the values of s vs. $\frac{\eta}{d_p^2 \rho} \frac{h}{S} \frac{\phi^2}{(1-\phi)^3}$ which has been calculated from the direct measurements of ϕ using the ultrasonic sensor. Fitting the Carman-Kozeny equation (Equation 2) to the data yields the ratio $E/\psi_p^2 \approx 272$ which is close to the value reported for other irregularly shaped beads [112]. SEM images (Figure 1) demonstrate that $CaCO_3$ particles used in this work have a similar shape regardless of particle size. Thus, we will consider $E/\psi_p^2 \approx 272$ as the reference value for all the samples. More-

20

over, heating the particles up to $T = 500°$C has no appreciable effect on their shape (see SEM pictures in Figures 10 and 11), thus we will also assume also $E/\psi_{\rm p}^2 \approx 272$ for the whole range of temperatures employed in our work.

Data on the particle volume fraction obtained as explained above are plotted in Figure 12 as a function of the previously imposed consolidation stress, average particle size and temperature. As would be expected for irregularly shaped adhesive particles subjected to relatively low consolidation stresses [113], the values of ϕ are well below the theoretical limit corresponding to the random loose packing of uniform, non-cohesive spheres ($\phi_{\rm RLP} \sim 0.55$) [114]. Regarding the evolution of ϕ with $\sigma_{\rm c}$ (for a given particle size and temperature), the powder bed becomes more compacted (ϕ increases) the larger the applied consolidation stress as would be expected. However, the influence of $\sigma_{\rm c}$ is less accused as the degree of compaction increases. Larger changes in ϕ are observed for $\sigma_{\rm c} \le 1000$ Pa whereas ϕ increases only slightly beyond this consolidation stress. This behavior can be satisfactorily described by a logarithmic law $\phi = c + d \ln \sigma_{\rm c}$ as also found for other powders tested at ambient temperature under similar ranges of consolidation stresses [115, 116].

Concerning the role of temperature (for a given $d_{\rm p}$), Figure 12 shows that the increase of temperature raises the powder compressibility (as measured by the slope $d = \Delta\phi / \ln \sigma_{\rm c}$). Thus, increasing values of T yield more porous (smaller ϕ) powder beds. This change in the micro-structure of the bed with T magnifies the effect of $\sigma_{\rm c}$ on ϕ. For the same range of consolidation stresses, the increase of ϕ becomes more pronounced as T increases. For

21

instance, for powders of $d_p \sim 45\,\mu$m, ϕ increases by around a 3% in the range $W \le \sigma_c \lessapprox 1000\,$Pa for $T = 25°$C whereas it is increased over a 14% if the bed is heated up to 500°C in the same range of consolidations.

Let us now focus on the effect of particle size on the compressibility of the powder. At a given temperature and consolidation stress, particles rearrange in more compact structures as d_p is increased. On the other hand, there exists a cross effect of d_p and T on ϕ. For example, for $\sigma_c \approx 1000\,$Pa, and when T is increased from 25 to 500°C, ϕ is reduced by a $\sim 11\%$ for $d_p \sim 80\,\mu$m, by a $\sim 18\%$ for $d_p \sim 60\,\mu$m, by a $\sim 20\%$ for $d_p \sim 45\,\mu$m, and by a $\sim 36\%$ for $d_p \sim 30\,\mu$m. This empirical observation can be quantified by the change of the values of d in the relationship $\phi = c + d \ln \sigma_c$ (see Table 3). As T is diminished, d decreases more markedly the smaller the particle size.

In summary, our experimental measurements show that $CaCO_3$ powders become less cohesive (smaller σ_t) and pack in closer structures (larger ϕ) more difficult to compress as d_p is increased. Conversely, as the cohesiveness of the powders increases because of a reduction of d_p, particles rearrange in more porous structures (smaller ϕ) which can be easily compressed even under low consolidation stresses. The increase of temperature magnifies these trends. As T raises, the powders become more cohesive and particles rearrange in more porous and easier to be compressed structures.

4. Discussion

4.1. Flowability of powders under small consolidations at room temperature

We will begin the discussion of our experimental results by analyzing the results on the tensile yield strength of $CaCO_3$ powder beds previously subjected to the small consolidation stress just given by their own weight per unit area ($\sigma_c = W$) at ambient temperature (Figure 4). Under these conditions, the flowability of powders depends mainly on the ratio of the attractive interparticle force F_{at} to particle weight mg, so-called cohesive granular Bond number [117],

$$Bo_g = \frac{F_{at}}{mg} \tag{3}$$

When the attractive force between particles is smaller than particle weight ($Bo_g < 1$), the powder flows freely. By contrast, powder flowability is hindered by the aggregative behavior of particles when the attractive interaction between them overcome their own weight ($Bo_g > 1$).

The attractive force between particles may be of capillary, magnetic, electrostatic and/or van der Waals nature [82, 118–120]. In our dry samples, capillary forces that would arise from water condensation on the particles surface [121] may be neglected. For non-charged fine powders, as our tested samples, the electrostatic force can be also dismissed as compared to the van der Waals force [122–124]. Nor our samples exhibit a magnetic behavior. Therefore, the attractive interaction between $CaCO_3$ particles is mainly due

to the short ranged van der Waals force $F_{at} = F_{vdW}$ which arises from the interaction between the fluctuating molecular dipoles of neighbor particles.

If dipole-dipole interaction is assumed pairwise and retardation effects are considered as negligible, the maximum van der Waals force between two unloaded particles at contact can be approximated by [125]:

$$F_{vdW} \approx \frac{AD^*}{20z_0^2}.$$

(4)

where A is the Hamaker constant, whose typical values are on the order of 10^{-19} J for most solids in vacuum [126], z_0 denotes the distance of closest approach between two molecules and ranges from 3 to 4 Å [122, 123, 127, 128], and $D^* = 2R^*$, being R^* the reduced local radius of curvature of the particles surfaces at contact. For smooth spherical beads of diameter d_p the reduced diameter is equal to $D^* = d_p/2$. The van der Waals force is however a short ranged interaction. Consequently, the magnitude of the van der Waals force is mainly determined by the roughness of the particles surface. Thus, d_p must be replaced by the typical size of the asperities d_{asp} ($D^* \approx d_{asp}^* = d_{asp}/2$). For particles of size on the order of tens of microns, a typical value of d_{asp} is $\sim 0.2\,\mu$m [129, 130]. Taking into account these considerations in Equation 4, the granular Bond number can be rewritten as

$$Bo_g \approx \frac{3Ad_{asp}}{20\pi gz_0^2\rho_p d_p^3}.$$

(5)

The above expression suggests that the cohesiveness of powders increases

greatly as d_p decreases as indicated by our measurements of the tensile yield strength (Figures 4 and 8). To quantify this observation, we have calculated Bo_g assuming $A \approx 1.01 \times 10^{-19}$ J for $CaCO_3$ [131] and $z_0 \approx 4$ Å, which give $Bo_g \sim 0.3$, $Bo_g \sim 1$, $Bo_g \sim 3$ and $Bo_g \sim 7$ for $d_p \sim 80\,\mu$m, $d_p \sim 60\,\mu$m, $d_p \sim 45\,\mu$m, and $d_p \sim 30\,\mu$m, respectively. As d_p is decreased from ~ 80 to $\sim 30\,\mu$m, the magnitude of the attractive force between particles gradually increases until it overcomes the particle weight. Thus, the increase of Bo_g yields an appreciable increase of cohesiveness of the $CaCO_3$ powders in this range of particle size as observed empirically therefore hindering their flowability.

The van der Waals force does not reflect however the remarkable increase of the tensile yield strength of the powder after it has been subjected to a consolidation stress as seen from our measurements (Figures 6 and 8). This effect is crucial for applications such as the CaL process where powder flow is to be resumed after the material has been consolidated under storage and at conditions possibly involving high temperatures [69]. Experimental results shown in the present work demonstrate that consolidation and high temperatures enhance significantly the powder tensile strength. Understanding the mechanisms that govern this undesirable behavior may provide us with useful methods to mitigate it. The next section is aimed at this purpose.

4.2. Microscopic forces between particles at contact under load

The flowability of powders ultimately depends on the microscopic forces among their particles. Thus, the tensile yield strength σ_t of a powder bed previously subjected to a consolidation stress σ_c stems from the average of the microscopic forces required to pull apart the particles at contact F_t (pull-off force) previously subjected to an external microscopic load force F_c.

When the compressive force F_c is small, the touching particles deform elastically (pure elastic contact [132, 133]). However, when the load force becomes large enough, some parts of the solid near the contact may exceed the elastic limit and deform plastically. If F_c continues increasing, the plastic zone expands inside the bulk of the particle until it eventually reaches the contact area and spreads along it. This is the elastic-plastic regime [132, 133].

Calculating the microscopic force required to separate the particles once an elastic-plastic contact is established is usually approached by two stages [82]. Firstly, particles partially deform plastically when subjected to an external F_c (indentation stage). Secondly, as the pull-off force is progressively increased, particles recover their profiles until they pull apart (decohesion stage). Thus, the maximum value of the pull-off force F_t does not only depend on the compression force but also on the physical properties of the particles at contact [134–136].

Mesarovic and Johnson analyzed the elastic-plastic contact between particles by means of an equivalent mechanical problem consisting of a frictionless contact between an elastic-plastic spherical particle and a rigid flat surface

26

(further details can be found in [82, 132–134, 137, 138]). Under this assumption, they were able to estimate F_t as

$$F_t = m_{EP} \sqrt{F_c} = \lambda \frac{2wE^*}{(\pi H^3)^{1/2}} \sqrt{F_c} \tag{6}$$

where w denotes the work of adhesion between the solid surfaces (defined as the work needed to separate two half-spaces to infinity in vacuum) which can be calculated as $w = 2\gamma$ for two surfaces of the same material; E^* is the reduced Young's modulus,

$$E^* = \left[\frac{1 - \nu_1^2}{E_1} + \frac{1 - \nu_2^2}{E_2} \right]^{-1} \tag{7}$$

being ν_i and E_i the Poisson ratio and the Young's modulus of the two solids (i=1,2) at contact, respectively; and λ is a parameter that depends on the dimensionless Tabor number [139]:

$$\mu = \left(\frac{d_{asp}^* w^2}{2 z_0^3 E^{*2}} \right)^{1/3} \tag{8}$$

Here $\lambda = 1$ for $\mu \ll 1$ (Derjaguin, Muller and Toporov -DMT- limit [140]) whereas $\lambda = 3/4$, if $\mu \gg 1$ (Johnson, Kendal and Roberts -JKR- limit [141]). At room temperature, we may use the central values of the physical properties reported for $CaCO_3$ in Table 1 (we also assume $z_0 \sim 4$ Å) to compute a Tabor number equals to $\mu \approx 0.77$ which lies between the JKR and DMT limits.

Equation 6 can be used as long as plastic deformation occurs between particles at contact. To find out if such type of deformation takes place (pure

elastic or elastic-plastic), two different criteria have been derived depending on the value of the dimensionless Tabor number. For $\mu \gg 1$, particles begin to flow plastically when the reduced radius of their asperities $d^*_{\text{asp}}/2$ is below [82, 142]

$$R_P^{JKR} = \frac{36M_0^3}{\pi^2} \left(\frac{wE^{*2}}{Y^3} \right)$$

(9)

where $M_0 \approx 0.447$ for $\nu = 0.28$ and $Y = H/2.8$. On the other hand, when $\mu \ll 1$, the onset of plasticity occurs if $d^*_{\text{asp}}/2$ is smaller than [82, 143]

$$R_P^{DMT} = \frac{12wE^{*2}}{\pi^2 K^3 Y^3}$$

(10)

being $K = 1.271 + 1.148\nu$. For $CaCO_3$ particles, $\mu \approx 0.77$ is between the JKR and DMT limits, thus the reduced radius which determines the limit between the elastic deformation and the onset of plasticity should range between those values predicted by Equations 9 and 10. At room temperature, assuming a reduced radius of asperities of $\sim 0.1\,\mu$m and using the reported values of the mechanical properties for $CaCO_3$ (Table 1) in the above expressions, we obtain $R_P^{JKR} \approx 1.77\,\mu$m and $R_P^{DMT} \approx 1.64\,\mu$m. Since these values are well above the typical radius of asperities, we may assume that $CaCO_3$ particles at contact deform plastically. Thus, Equation 6 can be used to predict the adhesive force between particles under load.

The average microscopic load force F_c and adhesion force F_t between the particles in our tests can be roughly estimated from the measurements of

the bulk consolidation stress σ_c and the tensile yield strength σ_t (Figure 8), respectively, using the averaging equation proposed by Rumpf [144]

$$F_i = \frac{\pi d_p^2}{\xi \phi} \sigma_i \qquad (11)$$

where F_i and σ_i are the microscopic contact force and the corresponding measured bulk stress (i=t,c), and ξ is the coordination number (defined as the number of contacts per particle) which can be derived from the particle volume fraction. Among all the existing relationships between ξ and ϕ [145], we will use that proposed by Nakagaki et al. [146]

$$\xi = \frac{\pi}{2}(1 - \phi)^{3/2} \qquad (12)$$

since the range of validity of this equation $0.18 < \phi$ fits well to the values of ϕ in the powder beds tested in the present work (Figure 12).

Figure 13 shows the computed values of the contact forces as depending on d_p and T for the tested $CaCO_3$ powders. Firstly, it is worth mentioning that, at a given temperature, and within the accuracy of our experimental results, data corresponding to particles of different size collapse into a single curve. Moreover, this curve is pretty well fitted by a linear relationship between F_t and $\sqrt{F_c}$ as would be expected from the elasto-plastic contact model (Equation 6). As also predicted by this equation, it is seen that the ratio $F_t/\sqrt{F_c}$ does only depend on the mechanical properties of the particles at contact regardless of particle size. Our experimental data is also in quan-

titative agreement with Equation 6. At room temperature, using the central values of the physical properties of $CaCO_3$ particles reported in Table 1, we may compute a theoretical slope $m_{EP} = F_t/\sqrt{F_c}$ ranging from 3.42 (for the JKR limit, $\lambda = 3/4$) to 4.56 $\sqrt{nN}$ (in the case of DMT limit, $\lambda = 1$) which are similar to the value obtained from the linear fitting of Equation 6 to our experimental results for $T = 25°C$ ($m_{exp} \approx 2.4\,\sqrt{nN}$, see Table 4).

Several issues would hinder however a closer agreement between theory and experiments. As previously mentioned, there exists a large degree of indeterminacy in the mechanical properties of $CaCO_3$ particles reported in literature (Table 1) which adds uncertainty to the calculated values of m_{EP}. Another rough approximation is the estimation of F_t and F_c from Equation 11. Rumpf's expression is strictly valid for hard monodisperse spherical particles and a random isotropic packing whereas our particles are irregularly shaped and their packing is not ideally isotropic. Finally, Equation 6 was derived for perfectly spherical and monodisperse particles at a single contact. However, $CaCO_3$ particles exhibit a small (albeit non neglegible) size dispersion (Figures 1 and 2). Furthermore, the contacts between particles may take place at multiple points involving several asperities. Nevertheless, despite all these approximations, it is remarkable that there exits a good agreement between the experimentally derived and the theoretically predicted values of the slope $F_t/\sqrt{F_c}$ at room temperature. On the basis of this agreement, it may be argued that Equation 6 can be a useful tool to envisage the effect of temperature on the cohesiveness of powders from the evolution with

temperature of fundamental mechanical properties of the solid.

As temperature increases, m_{exp} is progressively increased (Table 4). This experimental observation would be explained, according to Equation 6, by a decrease of the mechanical hardness of $CaCO_3$ particles with temperature as reported elsewhere [147]. Likewise, it might be foreseen from Equation 6 that an increase of the work of adhesion and the Young's modulus with temperature would enhance the interparticle adhesion force although we have not found in the literature any report on how these mechanical properties change with T for $CaCO_3$.

5. Conclusions

Energy storage using granular solids in CSP plants is gaining attention in the last years as a cheap and potentially efficient technique to overcome the intrinsic variability of direct solar irradiation. Solar energy can be stored in granular solids as sensible heat or in thermochemical form. In both cases large amounts of solids must be circulated through the plant and stored in silos at high temperature. So far, most experimental works focused on this subject have analyzed relevant physical properties of the solids to store energy such as heat transfer and important chemical aspects such as the chemical reactivity of the solids when subjected to multiple cycles in the case of thermochemical energy storage. Using results from these studies process simulations have been carried out to analyze the overall plant efficiency. However, a critical issue for heat storage in granular solids until now dismissed is how the

cohesiveness of the material changes with temperature as it may determine crucially the flowability of the solids in the process. As the cohesiveness of the powder is increased particles rearrange in more porous structures which can be easily compressed. As well known from industrial applications using granular solids, poor flowability caused by particle aggregation and jamming may cause serious problems in practice.

In this work we have measured the tensile yield strength and packing fraction of $CaCO_3$ powders with well-defined particle size in the range between ~ 30 and $\sim 80\,\mu$m of interest for the integration of the CaL process in CSP plants to store energy in thermochemical form. The results demonstrate that particle size determines critically the flow behavior of these powders as depending on temperature. As particle size is decreased below $\sim 80\,\mu$m powder cohesiveness is markedly promoted when temperature is increased above 100°C. Cohesiveness is significantly enhanced with temperature when the powders are subjected to relatively small consolidation stresses especially in the case of the finest samples.

In our work we have also analyzed the physical mechanisms by which the cohesive behavior of granular solids is enhanced with temperature. To this end the average forces of consolidation and adhesion between individual particles have been estimated from the measured bulk stresses and particle volume fraction. The results show that the interparticle force of adhesion F_t scales proportionally to the square root of the interparticle consolidation force F_c in agreement with a contact model based on the assumption that the

solid near the interparticle contact zone yields plastically. As temperature increases, the rate of increase of F_t with $\sqrt{F_c}$ is progressively increased which may be explained by a decrease of the mechanical hardness of the solid as measured elsewhere.

A main conclusion from our work is that the change of flowability of granular materials with temperature is not only affected critically by particle size but also by the variation of the solid mechanical properties with temperature. The results presented here would be useful in general for applications involving the storage and transport of granular solids at high temperature. They may help develop methods for mitigating the possible significant increase of powder cohesiveness with temperature (as found in our work for $CaCO_3$ powders) for example by preparing functional particles with enhanced mechanical hardness at high temperature.

References

[1] O. Edenhofer, R. P. Madruga, Y. Sokona, K. Seyboth, P. Eickemeier, P. Matschoss, G. Hansen, S. Kadner, S. Schlmer, T. Zwickel, C. von Stechow (Eds.), Renewable Energy Sources and Climate Change Mitigation. Special Report of the Intergovernmental Panel on Climate Change, Cambridge University Press, 2012.

[2] S. Chu, A. Majumdar, Opportunities and challenges for a sustainable energy future, Nature 488 (2012) 294–303. doi:https://doi.org/10.1038/nature11475.

[3] G. Crabtree, Perspective: The energy-storage revolution, Nature 526 (2015) S92. doi:https://doi.org/10.1038/526S92a.

[4] D. Lindley, Smart grids: The energy storage problem, Nature 463 (2010) 18–20. doi:https://doi.org/10.1038/463018a.

[5] M. Z. Jacobson, Review of solutions to global warming, air pollution, and energy security, Energy Environ. Sci. 2 (2009) 148–173. doi:https://doi.org/10.1039/B809990C.

[6] Y. Tian, C. Zhao, A review of solar collectors and thermal energy storage in solar thermal applications, Appl. Energy 104 (2013) 538–553. doi:https://doi.org/10.1016/j.apenergy.2012.11.051.

[7] M. Romero, A. Steinfeld, Concentrating solar thermal power and thermochemical fuels, Energy Environ. Sci. 5 (2012) 9234–9245. doi:https://doi.org/10.1039/C2EE21275G.

[8] J. T. Hinkley, J. A. Hayward, B. Curtin, A. Wonhas, R. Boyd, C. Grima, A. Tadros, R. Hall, K. Naicker, An analysis of the costs and opportunities for concentrating solar power in Australia, Renew. Energ. 57 (2013) 653–661. doi:https://doi.org/10.1016/j.renene.2013.02.020.

[9] V. S. Reddy, S. Kaushik, K. Ranjan, S. Tyagi, State-of-the-art of solar thermal power plants - A review, Renew. Sust. Energ. Rev. 27 (2013) 258–273. doi:https://doi.org/10.1016/j.rser.2013.06.037.

[10] S. Kuravi, J. Trahan, D. Y. Goswami, M. M. Rahman, E. K. Stefanakos, Thermal energy storage technologies and systems for concentrating solar power plants, Prog. Energy Combust. Sci. 39 (4) (2013) 285–319. doi:https://doi.org/10.1016/j.pecs.2013.02.001.

[11] H. L. Zhang, J. Baeyens, J. Degreve, G. Caceres, Concentrated solar power plants: Review and design methodology, Renew. Sust. Energ. Rev. 22 (2013) 466–481. doi:https://doi.org/10.1016/j.rser.2013.01.032.

[12] A. Henry, R. Prasher, The prospect of high temperature solid state energy conversion to reduce the cost of concen-

trated solar power, Energy Environ. Sci. 7 (2014) 1819–1828. doi:https://doi.org/10.1039/C4EE00288A.

[13] S. Pintaldi, C. Perfumo, S. Sethuvenkatraman, S. White, G. Rosengarten, A review of thermal energy storage technologies and control approaches for solar cooling, Renew. Sust. Energ. Rev. 41 (2015) 975–995. doi:https://doi.org/10.1016/j.rser.2014.08.062.

[14] M. Becker, Comparison of heat transfer fluids for use in solar thermal power stations, Electr. Pow. Syst. Res. 3 (3) (1980) 139–150. doi:https://doi.org/10.1016/0378-7796(80)90001-2.

[15] M. J. Bignon, The influence of the heat transfer fluid on the receiver design, Electr. Pow. Syst. Res. 3 (1) (1980) 99–109. doi:https://doi.org/10.1016/0378-7796(80)90026-7.

[16] D. Barlev, R. Vidu, P. Stroeve, Innovation in concentrated solar power, Sol. Energy Mater. Sol. Cells 95 (10) (2011) 2703–2725. doi:https://doi.org/10.1016/j.solmat.2011.05.020.

[17] G. J. Janz, C. B. Allen, N. P. Bansal, R. M. Murphy, R. P. T.Tomkins, Physical properties data compilations relevant to energy storage. II. Molten salts: data on single and multi-components salt systems, Tech. rep., National Standard Reference Data System (1979). doi:https://doi.org/10.6028/NBS.NSRDS.61p2.

[18] A. G. Fernandez, S. Ushak, H. Galleguillos, F. J. Perez, Development of new molten salts with LiNO3 and Ca(NO3)2 for energy storage in CSP plants, Appl. Energy 119 (2014) 131–140. doi:https://doi.org/10.1016/j.apenergy.2013.12.061.

[19] J. Ortega, J. Burgaleta, F. M. Tellez, Central Receiver System Solar Power Plant Using Molten Salt as Heat Transfer Fluid, ASME. J. Sol. Energy Eng. 130 (2) (2018) 024501–6. doi:https://doi.org/10.1115/1.2807210.

[20] R. I. Dunn, P. J. Hearps, M. N. Wright, Molten-salt power towers: Newly commercial concentrating solar storage, Proc. IEEE 100 (2) (2012) 504–515. doi:https://doi.org/10.1109/JPROC.2011.2163739.

[21] K. Vignarooban, X. Xu, A. Arvay, K. Hsu, A. M. Kannan, Heat transfer fluids for concentrating solar power systems A review, Appl. Energy 146 (2015) 383–396. doi:https://doi.org/10.1016/j.apenergy.2015.01.125.

[22] E. Pihl, D. Kushnir, B. Sanden, F. Johnsson, Material constraints for concentrating solar thermal power, Energy 44 (1) (2012) 944–954. doi:https://doi.org/10.1016/j.energy.2012.04.057.

[23] S. Khare, M. Dell'Amico, C. Knight, S. McGarry, Selection of materials for high temperature sensible energy stor-

age, Sol. Energy Mater. Sol. Cells 115 (2013) 114–122. doi:https://doi.org/10.1016/j.solmat.2013.03.009.

[24] G. Flamant, Theoretical and experimental study of radiant heat transfer in a solar fluidized-bed receiver, AIChE J. 28 (4) (1982) 529–535. doi:https://doi.org/10.1002/aic.690280402.

[25] D. M. Bachovchin, D. H. Archer, D. H. Neale, Heat transfer in a fluidized-bed solar thermal receiver, AIChE Symp. Ser. (1983) 222.

[26] I. Haddad, M. Elsayed, Transient performance of fluidized bed solar receiver at various parametric conditions, Solar & Wind Technol. 5 (6) (1988) 653–659. doi:https://doi.org/10.1016/0741-983X(88)90063-X.

[27] S. Ayyappan, K. Mayilsamy, V. Sreenarayanan, Performance improvement studies in a solar greenhouse drier using sensible heat storage materials, Heat Mass Transf. 52 (3) (2016) 459–467. doi:https://doi.org/10.1007/s00231-015-1568-5.

[28] I. Sarbu, C. Sebarchievici, A Comprehensive Review of Thermal Energy Storage, Sustainability 10 (1) (2018) 1–32. doi:https://doi.org/10.3390/su10010191.

[29] A. Sharma, V. Tyagi, C. Chen, D. Buddhi, Review on thermal energy storage with phase change materials and applications, Renew. Sust. Energ. Rev. 13 (2) (2009) 318–345. doi:https://doi.org/10.1016/j.rser.2007.10.005.

[30] S. M. Hasnain, Review on sustainable thermal energy storage technologies, Part I: heat storage materials and techniques, Energy Convers. Manag. 39 (11) (1998) 1127–1138. doi:https://doi.org/10.1016/S0196-8904(98)00025-9.

[31] U. Herrmann, D. W. Kearney, Survey of Thermal Energy Storage for Parabolic Trough Power Plants, ASME. J. Sol. Energy Eng. 124 (2) (2002) 145–152. doi:https://doi.org/10.1115/1.1467601.

[32] A. Kasaeian, L. Bahrami, F. Pourfayaz, E. Khodabandeh, W.-M. Yan, Experimental studies on the applications of PCMs and nano-PCMs in buildings: A critical review, Energy Build. 154 (2017) 96–112. doi:https://doi.org/10.1016/j.enbuild.2017.08.037.

[33] P. Tatsidjodoung, N. L. Pierres, L. Luo, A review of potential materials for thermal energy storage in building applications, Renew. Sust. Energ. Rev. 18 (2013) 327–349. doi:https://doi.org/10.1016/j.rser.2012.10.025.

[34] P. Pardo, A. Deydier, Z. Anxionnaz-Minvielle, S. Rouge, M. Cabassud, P. Cognet, A review on high temperature thermochemical heat energy storage, Renew. Sust. Energ. Rev. 32 (2014) 591–610. doi:https://doi.org/10.1016/j.rser.2013.12.014.

[35] H. O. Paksoy, Thermal energy storage for sustainable energy consup-

tion, Springer: Netherlands, 2007. doi:https://doi.org/10.1007/978-1-4020-5290-3.

[36] K. E. N'Tsoukpoe, H. Liu, N. L. Pierres, L. Luo, A review on long-term sorption solar energy storage, Renew. Sust. Energ. Rev. 13 (9) (2009) 2385–2396. doi:https://doi.org/10.1016/j.rser.2009.05.008.

[37] T. M. I. Mahlia, T. J. Saktisahdan, A. Jannifar, M. H. Hasan, H. S. C. Matseelar, A review of available methods and development on energy storage; technology update, Renew. Sust. Energ. Rev. 33 (2014) 532–545. doi:https://doi.org/10.1016/j.rser.2014.01.068.

[38] C. Prieto, P. Cooper, A. I. Fernandez, L. F. Cabeza, Review of technology: Thermochemical energy storage for concentrated solar power plants, Renew. Sust. Energ. Rev. 60 (2016) 909–929. doi:https://doi.org/10.1016/j.rser.2015.12.364.

[39] I. Dincer, M. A. Rosen, Thermal Energy Storage: Systems and Applications, 2nd Edition, John Wiley & Sons, 2010.

[40] P. Pinel, C. A. Cruickshank, I. Beausoleil-Morrison, A. Wills, A review of available methods for seasonal storage of solar thermal energy in residential applications, Renew. Sust. Energ. Rev. 15 (7) (2011) 3341–3359. doi:https://doi.org/10.1016/j.rser.2011.04.013.

[41] Y. Kato, Thermal Energy Storage for Sustainable Energy Consumption. NATO Science Series (Mathematics, Physics and Chem-

istry), Vol. 234, Springer, Dordrecht, 2007, Ch. Chemical energy conversion technologies for efficient energy use, pp. 377–391. doi:https://doi.org/10.1007/978-1-4020-5290-3.

[42] A. H. Abedin, M. A. Rosen, A Critical Review of Thermochemical Energy Storage Systems, Open Renew. Energy J. 4 (2011) 42–46. doi:http://dx.doi.org/10.2174/1876387101004010042.

[43] L. F. Cabeza, C. Sole, A. Castell, E. Oro, A. Gil, Review of solar thermal storage techniques and associated heat transfer technologies, Proc. IEEE 100 (2) (2012) 525–538. doi:https://doi.org/10.1109/JPROC.2011.2157883.

[44] K. J. Albrecht, G. S. Jackson, R. J. Braun, Thermodynamically consistent modeling of redox-stable perovskite oxides for thermochemical energy conversion and storage, Appl. Energy 165 (2016) 285–296. doi:https://doi.org/10.1016/j.apenergy.2015.11.098.

[45] L. F. Cabeza, A. Sole, X. Fontanet, C. Barreneche, A. Jove, M. Gallas, C. Prieto, A. I. Fernandez, Thermochemical energy storage by consecutive reactions for higher efficient concentrated solar power plants (CSP): Proof of concept, Appl. Energy 185 (2017) 836–845. doi:https://doi.org/10.1016/j.apenergy.2016.10.093.

[46] S. Tescari, A. Singh, C. Agrafiotis, L. de Oliveira, S. Breuer, B. Schlgl-Knothe, M. Roeb, C. Sattler, Experimental evalua-

tion of a pilot-scale thermochemical storage system for a concentrated solar power plant, Appl. Energy 189 (2017) 66–75. doi:https://doi.org/10.1016/j.apenergy.2016.12.032.

[47] R. Chacartegui, A. Alovisio, C. Ortiz, J. M. Valverde, V. Verda, J. A. Becerra, Thermochemical energy storage of concentrated solar power by integration of the calcium looping process and a CO2 power cycle, Appl. Energy 173 (2016) 589–605. doi:https://doi.org/10.1016/j.apenergy.2016.04.053.

[48] R. Barker, Reversibility of the reaction CaCO3–CaO–CO2, J. Appl. Chem. Biotechnol. 23 (10) (1973) 733–742. doi:https://doi.org/10.1002/jctb.5020231005.

[49] R. Barker, The reactivity of calcium oxide towards carbon dioxide and its use for energy storage, J. Appl. Chem. Biotech. 24 (4-5) (1974) 221–227. doi:https://doi.org/10.1002/jctb.2720240405.

[50] G. Flamant, D. Hernandez, C. Bonet, J.-P. Traverse, Experimental aspects of the thermochemical conversion of solar energy; Decarbonation of CaCO3, Sol. Energy 24 (4) (1980) 385–395. doi:https://doi.org/10.1016/0038-092X(80)90301-1.

[51] C. Ortiz, J. Valverde, R. Chacartegui, L. Perez-Maqueda, P. Gimenez, The Calcium-Looping (CaCO3/CaO) Process for Thermochemical Energy Storage in Concentrating Solar

Power Plants, Renew. Sust. Energ. Rev. 113 (2019) 109252. doi:https://doi.org/10.1016/j.rser.2019.109252.

[52] T. Shimizu, T. Hirama, H. Hosoda, K. Kitano, M. Inagaki, K. Tejima, A Twin Fluid-Bed Reactor for Removal of CO2 from Combustion Processes, Chem. Eng. Res. Des. 77 (1) (1999) 62–68. doi:https://doi.org/10.1205/026387699525882.

[53] A. M. Kierzkowska, R. Pacciani, C. R. Mller, CaO-Based CO2 Sorbents: From Fundamentals to the Development of New, Highly Effective Materials, ChemSusChem 6 (7) (2013) 1130–1148. doi:https://doi.org/10.1002/cssc.201300178.

[54] J. M. Valverde, Ca-based synthetic materials with enhanced CO2 capture efficiency, J. Mater. Chem. A 1 (2013) 447–468. doi:https://doi.org/10.1039/C2TA00096B.

[55] J. Blamey, E. J. Anthony, J. Wang, P. S. Fennell, The calcium looping cycle for large-scale CO2 capture, Prog. Energy Combust. Sci. 36 (2) (2010) 260–279. doi:https://doi.org/10.1016/j.pecs.2009.10.001.

[56] A. Perejon, L. M. Romeo, Y. Lara, P. Lisbona, A. Martinez, J. M. Valverde, The Calcium-Looping technology for CO2 capture: On the important roles of energy integration and sorbent behavior, Appl. Energy 162 (2016) 787–807. doi:https://doi.org/10.1016/j.apenergy.2015.10.121.

[57] R. Chacartegui, J. A. Becerra, J. M. Valverde, C. Ortiz, A. Alovisio, Integrated calcination-carbonation system and closed-loope CO2 cycle for thermochemical energy storage and electric energy generation (2016).

[58] A. Meier, N. Gremaud, A. Steinfeld, Economic evaluation of the industrial solar production of lime, Energy Convers. Manag. 46 (6) (2005) 905–926. doi:https://doi.org/10.1016/j.enconman.2004.06.005.

[59] C. Dean, J. Blamey, N. Florin, M. Al-Jeboori, P. Fennell, The calcium looping cycle for CO2 capture from power generation, cement manufacture and hydrogen production, Chem. Eng. Res. Des. 89 (6) (2011) 836–855. doi:https://doi.org/10.1016/j.cherd.2010.10.013.

[60] K. Atsonios, P. Grammelis, S. Antiohos, N. Nikolopoulos, E. Kakaras, Integration of calcium looping technology in existing cement plant for CO2 capture: Process modeling and technical considerations, Fuel 153 (2015) 210–223. doi:https://doi.org/10.1016/j.fuel.2015.02.084.

[61] M. Spinelli, I. Martinez, M. C. Romano, One-dimensional model of entrained-flow carbonator for CO2 capture in cement kilns by Calcium looping process, Chem. Eng. Sci. 191 (2018) 100–114. doi:https://doi.org/10.1016/j.ces.2018.06.051.

[62] J. Plou, I. Martinez, G. S. Grasa, R. Murillo, Experimental carbonation

of CaO in an entrained flow reactor, React. Chem. Eng. 4 (2019) 899–908. doi:https://doi.org/10.1039/C9RE00015A.

[63] B. Arias, M. E. Diego, J. C. Abanades, M. Lorenzo, L. Diaz, D. Martinez, J. Alvarez, A. Sanchez-Biezma, Demonstration of steady state CO2 capture in a 1.7MWth calcium looping pilot, Int. J. Greenh. Gas Con. 18 (2013) 237–245. doi:https://doi.org/10.1016/j.ijggc.2013.07.014.

[64] H. Dieter, C. Hawthorne, M. Zieba, G. Scheffknecht, Progress in Calcium Looping Post Combustion CO2 Capture: Successful Pilot Scale Demonstration, Energy Procedia 37 (2013) 48–56, GHGT-11 Proceedings of the 11th International Conference on Greenhouse Gas Control Technologies, 18-22 November 2012, Kyoto, Japan. doi:https://doi.org/10.1016/j.egypro.2013.05.084.

[65] J. Strohle, M. Junk, J. Kremer, A. Galloy, B. Epple, Carbonate looping experiments in a 1MWth pilot plant and model validation, Fuel 127 (2014) 13–22. doi:https://doi.org/10.1016/j.fuel.2013.12.043.

[66] D. P. Hanak, E. J. Anthony, V. Manovic, A review of developments in pilot-plant testing and modelling of calcium looping process for CO2 capture from power generation systems, Energy Environ. Sci. 8 (2015) 2199–2249. doi:https://doi.org/10.1039/C5EE01228G.

[67] R. H. Borgwardt, Sintering of nascent calcium oxide, Chem. Eng. Sci.

44 (1) (1989) 53–60. doi:https://doi.org/10.1016/0009-2509(89)85232-7.

[68] J. Wang, V. Manovic, Y. Wu, E. J. Anthony, A study on the activity of CaO-based sorbents for capturing CO2 in clean energy processes, Appl. Energy 87 (4) (2010) 1453–1458. doi:https://doi.org/10.1016/j.apenergy.2009.08.010.

[69] C. Ortiz, M. Romano, J. Valverde, M. Binotti, R. Chacartegui, Process integration of Calcium-Looping thermochemical energy storage system in concentrating solar power plants, Energy 155 (2018) 535–551. doi:https://doi.org/10.1016/j.energy.2018.04.180.

[70] A. Perejon, J. M. Valverde, J. Miranda-Pizarro, P. E. Sanchez-Jimenez, L. A. Perez-Maqueda, Large-Scale Storage of Concentrated Solar Power from Industrial Waste, ACS Sustain. Chem. Eng. 5 (3) (2017) 2265–2272. doi:https://doi.org/10.1021/acssuschemeng.6b02576.

[71] B. Sarrion, J. M. Valverde, A. Perejon, L. Perez-Maqueda, P. E. Sanchez-Jimenez, On the Multicycle Activity of Natural Limestone/Dolomite for Thermochemical Energy Storage of Concentrated Solar Power, Energy Technol. 4 (8) (2016) 1013–1019. doi:https://doi.org/10.1002/ente.201600068.

[72] Solar Calcium Looping Integration for Thermochemical Energy Storage (SOCRATCES). Horizon 2020 project. The EU Framework

Programme for Research and Innovation, ref.3228/0666.

URL https://cordis.europa.eu/project/rcn/212577/factsheet/en

[73] A. Muto, T. Hansen, Demonstration of High-Temperature Calcium-Based Thermochemical Energy Storage System for use with Concentrating Solar Power Facilities, Tech. Rep. EE0007116, Southern Research Institute, Golden, CO (United States) (2019). doi:https://doi.org/10.2172/1501361.

[74] S. K. Gangwal, Final Technical Report Project Regenerative Carbonate-Based Thermochemical Energy Storage System for Concentrating Solar Power, Tech. Rep. EE0006535, Southern Research Institute (2016).

[75] D. Kunii, O. Levenspiel, H. Brenner, Fluidization Engineering, Butterworth-Heinemann-series in chemical engineering, Elsevier Science, 1991. doi:https://doi.org/10.1016/C2009-0-24190-0.

[76] J. M. Valverde, A. Castellanos, P. Mills, M. A. S. Quintanilla, Effect of particle size and interparticle force on the fluidization behavior of gas-fluidized beds, Phys. Rev. E 67 (2003) 051305. doi:https://doi.org/10.1103/PhysRevE.67.051305.

[77] J. C. Abanades, D. Alvarez, Conversion Limits in the Reaction of CO2 with Lime, Energy Fuels 17 (2) (2003) 308–315. doi:https://doi.org/10.1021/ef020152a.

[78] G. S. Grasa, J. C. Abanades, M. Alonso, B. Gonzalez, Reactivity of highly cycled particles of CaO in a carbonation/calcination loop, Chem. Eng. J. 137 (3) (2008) 561–567. doi:https://doi.org/10.1016/j.cej.2007.05.017.

[79] G. Grasa, R. Murillo, M. Alonso, J. C. Abanades, Application of the random pore model to the carbonation cyclic reaction, AIChE J. 55 (5) (2009) 1246–1255. doi:https://doi.org/10.1002/aic.11746.

[80] I. Martinez, C. Grasa, R. Murillo, B. Arias, J. C. Abanades, Kinetics of Calcination of Partially Carbonated Particles in a Ca-Looping System for CO2 Capture, Energy Fuels 26 (2) (2012) 1432–1440. doi:https://doi.org/10.1021/ef201525k.

[81] M. Benitez-Guerrero, B. Sarrion, A. Perejon, P. E. Sanchez-Jimenez, L. A. Perez-Maqueda, J. M. Valverde, Large-scale high-temperature solar energy storage using natural minerals, Sol. Energy Mater. Sol. Cells 168 (2017) 14–21. doi:https://doi.org/10.1016/j.solmat.2017.04.013.

[82] A. Castellanos, The relationship between attractive interparticle forces and bulk behaviour in dry and uncharged fine powders, Adv. Phys. 54 (4) (2005) 263–376. doi:https://doi.org/10.1080/17461390500402657.

[83] D. Geldart, Types of gas fluidization, Powder Technol. 7 (5) (1973) 285–292. doi:https://doi.org/10.1016/0032-5910(73)80037-3.

[84] J. M. Valverde, M. A. S. Quintanilla, A. Castellanos, Jamming threshold of dry fine powders, Phys. Rev. Lett. 92 (2004) 258303. doi:https://doi.org/10.1103/PhysRevLett.92.258303.

[85] B. Arias, M. Alonso, C. Abanades, CO2 Capture by Calcium Looping at Relevant Conditions for Cement Plants: Experimental Testing in a 30 kWth Pilot Plant, Ind. Eng. Chem. Res. 56 (10) (2017) 2634–2640. doi:https://doi.org/10.1021/acs.iecr.6b04617.

[86] A. Castellanos, J. M. Valverde, M. A. S. Quintanilla, Aggregation and sedimentation in gas-fluidized beds of cohesive powders, Phys. Rev. E 64 (2001) 041304.

[87] U. Zafar, V. Vivacqua, G. Calvert, M. Ghadiri, J. A. S. Cleaver, A review of bulk powder caking, Powder Technol 313 (2017) 389–401. doi:https://doi.org/10.1016/j.powtec.2017.02.024.

[88] I. Tomasetta, D. Barletta, M. Poletto, The Effect of Temperature on Flow Properties of Fine Powders, Chem. Eng. Trans. 24 (2011) 655–660. doi:https://doi.org/10.3303/CET1124110.

[89] H. Purutyan, B. H. Pittenger, J. W. Carson, Six steps to designing a storage vessel that really works, Powder Bulk Eng. 13 (1999) 56–67.

[90] G. Moumin, S. Tescari, P. Sundarraj, L. de Oliveira, M. Roeb, C. Sattler, Solar treatment of cohesive particles in a di-

rectly irradiated rotary kiln, Sol. Energy 182 (2019) 480–490. doi:https://doi.org/10.1016/j.solener.2019.01.093.

[91] [link].

URL https://www.ksl-staubtechnik.de/en/pruefentesten/fractions/

[92] H. Shi, R. Mohanty, S. Chakravarty, R. Cabiscol, M. Morgeneyer, H. Zetzener, J. Y. Ooi, A. Kwade, S. Luding, V. Magnanimo, Effect of Particle Size and Cohesion on Powder Yielding and Flow, KONA Powder Part. J. (2018) 226–250doi:10.14356/kona.2018014.

[93] L. Riester, P. Blau, E. Lara-Curzio, K. Breder, Nanoindentation with a Knoop indenter, Thin Solid Films 377-378 (2000) 635–639. doi:https://doi.org/10.1016/S0040-6090(00)01298-0.

[94] L. Zheng, A. W. Schmid, J. C. Lambropoulos, Surface effects on Youngs modulus and hardness of fused silica by nanoindentation study, J. Mater. Sci. 42 (2007) 191–198. doi:https://doi.org/10.1007/s10853-006-1051-2.

[95] W. C. Oliver, G. M. Pharr, An improved technique for determining hardness and elastic modulus using load and displacement sensing indentation experiments, J. Mater. Res. 7 (6) (1992) 1564–1583. doi:https://doi.org/10.1557/JMR.1992.1564.

[96] J. M. Valverde, A. Castellanos, A. Ramos, A. T. Perez, M. A. Morgan, P. K. Watson, An automated apparatus for

measuring the tensile strength and compressibility of fine cohesive powders, Rev. Sci. Instrum. 71 (7) (2000) 2791–2795. doi:https://doi.org/10.1063/1.1150694.

[97] J. Schwedes, Review on testers for measuring flow properties of bulk solids, Granul. Matter 5 (1) (2003) 1–43. doi:https://doi.org/10.1007/s10035-002-0124-4.

[98] A. Castellanos, J. M. Valverde, M. A. S. Quintanilla, The Sevilla Powder Tester: A Tool for Characterizing the Physical Properties of Fine Cohesive Powders at Very Small Consolidations, KONA Powder Part. J. 22 (2004) 66–81. doi:https://doi.org/10.14356/kona.2004011.

[99] U. Zafar, C. Hare, G. Calvert, M. Ghadiri, R. Girimonte, B. Formisani, M. A. S. Quintanilla, J. M. Valverde, Comparison of cohesive powder flowability measured by Schulze Shear Cell, Raining Bed Method, Sevilla Powder Tester and new Ball Indentation Method, Powder Technol. 286 (2015) 807–816. doi:https://doi.org/10.1016/j.powtec.2015.09.010.

[100] Y. Chen, M. A. S. Quintanilla, J. Yang, J. M. Valverde, R. N. Dave, Pull-off force of coated fine powders under small consolidation, Phys. Rev. E 79 (2009) 041305. doi:https://doi.org/10.1103/PhysRevE.79.041305.

[101] D. Barletta, M. Poletto, A. C. Santomaso, Chapter 4 Bulk Pow-

der Flow Characterisation Techniques, in: A. Hassanpour, C. Hare, M. Pasha (Eds.), Powder Flow: Theory, Characterisation and Application, The Royal Society of Chemistry, 2019, pp. 64–146. doi:https://doi.org/10.1039/9781788016100-00064.

[102] J. M. Valverde, A. Castellanos, P. K. Watson, The effect of particle size on interparticle adhesive forces for small loads, Powder Technol. 118 (3) (2001) 236–241. doi:https://doi.org/10.1016/S0032-5910(00)00382-X.

[103] H. Schubert, Capillary forces - modeling and application in particulate technology, Powder Technol. 37 (1) (1984) 105–116. doi:https://doi.org/10.1016/0032-5910(84)80010-8.

[104] J. M. Valverde, F. Raganati, M. A. S. Quintanilla, J. M. P. Ebri, P. Ammendola, R. Chirone, Enhancement of CO2 capture at Ca-looping conditions by high-intensity acoustic fields, Appl. Energy 111 (2013) 538–549. doi:https://doi.org/10.1016/j.apenergy.2013.05.012.

[105] J. M. Valverde, A. Castellanos, M. A. S. Quintanilla, The memory of granular materials, Contemp. Phys. 44 (5) (2003) 389–399. doi:https://doi.org/10.1080/0010751031000155939.

[106] P. C. Carman, Fluid flow through granular beds, Trans. Inst. Chem. Eng. 15 (1937) 150–166.

[107] R. M. Nedderman, Statics and Kinematics of Gran-

ular Materials, Cambridge University Press, 1992. doi:https://doi.org/10.1017/CBO9780511600043.

[108] S. C. Tsinontides, R. Jackson, The mechanics of gas fluidized beds with an interval of stable fluidization, J. Fluid Mech. 255 (1993) 237–274. doi:https://doi.org/10.1017/S0022112093002472.

[109] J. M. Valverde, A. Ramos, A. Castellanos, P. K. Watson, The tensile strength of cohesive powders and its relationship to consolidation, free volume and cohesivity, Powder Technol. 97 (3) (1998) 237–245. doi:https://doi.org/10.1016/S0032-5910(98)00025-4.

[110] M. A. S. Quintanilla, J. M. Valverde, A. Castellanos, Adhesion force between fine particles with controlled surface properties, AIChE J. 52 (5) (2006) 1715–1728. doi:https://doi.org/10.1002/aic.10770.

[111] Y. A. Criado, B. Arias, J. C. Abanades, Calcium looping CO2 capture system for back-up power plants, Energy Environ. Sci. 10 (2017) 1994–2004. doi:http://dx.doi.org/10.1039/C7EE01505D.

[112] M. J. Espin, M. A. S. Quintanilla, J. M. Valverde, Effect of particle size polydispersity on the yield stress of magnetofluidized beds as depending on the magnetic field orientation, Chem. Eng. J. 277 (2015) 269–285. doi:https://doi.org/10.1016/j.cej.2015.04.124.

[113] J. M. Valverde, A. Castellanos, Random loose packing of cohesive

granular materials, Europhysics Letters (EPL) 75 (6) (2006) 985–991. doi:https://doi.org/10.1209/epl/i2006-10208-4.

[114] D. Bideau, A. Hansen, Disorder and Granular Media, North-Holland, Amsterdam, 1993.

[115] P. K. Watson, J. M. Valverde, A. Castellanos, The tensile strength and free volume of cohesive powders compressed by gas flow, Powder Technol. 115 (1) (2001) 45–50. doi:https://doi.org/10.1016/S0032-5910(00)00275-8.

[116] K. H. Roscoe, A. N. Schofield, C. P. Wroth, On The Yielding of Soils, Gotechnique 8 (1) (1958) 22–53. doi:http://doi.org/10.1680/geot.1958.8.1.22.

[117] S. T. Nase, W. L. Vargas, A. A. Abatan, J. J. McCarthy, Discrete characterization tools for cohesive granular material, Powder Technol. 116 (2) (2001) 214–223. doi:https://doi.org/10.1016/S0032-5910(00)00398-3.

[118] J. Visser, Van der Waals and other cohesive forces affecting powder fluidization, Powder Technol. 58 (1) (1989) 1–10. doi:https://doi.org/10.1016/0032-5910(89)80001-4.

[119] J. P. K. Seville, C. D. Willett, P. C. Knight, Interparticle forces in fluidisation: a review, Powder Technol. 113 (3) (2000) 261–268. doi:https://doi.org/10.1016/S0032-5910(00)00309-0.

[120] S. J. Antony, W. Hoyle, Y. Ding (Eds.), Granular Materials: Fundamentals and Applications, The Royal Society of Chemistry, 2004. doi:https://doi.org/10.1039/9781847550996.

[121] S. Herminghaus, Dynamics of wet granular matter, Adv. Phys. 54 (3) (2005) 221–261. doi:https://doi.org/10.1080/00018730500167855.

[122] H. Krupp, Particle adhesion theory and experiment, Adv. Colloid Interface Sci. 1 (2) (1967) 111–239. doi:https://doi.org/10.1016/0001-8686(67)80004-6.

[123] K. Rietema, The Dynamics of Fine Powders, Springer Netherlands, 1991. doi:https://doi.org/10.1007/978-94-011-3672-3.

[124] B. Gady, D. Schleef, R. Reifenberger, D. Rimai, L. P. DeMejo, Identification of electrostatic and van der Waals interaction forces between a micrometer-size sphere and a flat substrate, Phys. Rev. B 53 (1996) 8065–8070. doi:https://doi.org/10.1103/PhysRevB.53.8065.

[125] H. C. Hamaker, The London-van der Waals attraction between spherical particles, Physica 4 (10) (1937) 1058–1072. doi:https://doi.org/10.1016/S0031-8914(37)80203-7.

[126] S. Ross, L. D. Morrison, Colloidal Systems and Interfaces, Wiley-Interscience, New York, USA, 1988.

[127] J. Israelachvili, Intermolecular and Surface Forces, Academic Press, New York, USA, 1992.

[128] N. Yu, A. A. Polycarpou, Adhesive contact based on the Lennard-Jones potential: a correction to the value of the equilibrium distance as used in the potential, J. Colloid Interface Sci. 278 (2) (2004) 428–435. doi:https://doi.org/10.1016/j.jcis.2004.06.029.

[129] L. Massimilla, G. Dons, Cohesive forces between particles of fluid-bed catalysts, Powder Technol. 15 (2) (1976) 253–260. doi:https://doi.org/10.1016/0032-5910(76)80054-X.

[130] E. R. Beach, G. W. Tormoen, J. Drelich, R. Han, Pull-off Force Measurements between Rough Surfaces by Atomic Force Microscopy, J. Colloid Interface Sci. 247 (1) (2002) 84–99. doi:https://doi.org/10.1006/jcis.2001.8126.

[131] L. Bergstrom, Hamaker constants of inorganic materials, Adv. Colloid Interface Sci. 70 (1997) 125–169. doi:https://doi.org/10.1016/S0001-8686(97)00003-1.

[132] S. D. Mesarovic, N. A. Fleck, Spherical indentation of elastic-plastic solids, Proc. R. Soc. Lond. A 455 (1987) (1999) 2707–2728. doi:https://doi.org/10.1098/rspa.1999.0423.

[133] S. D. Mesarovic, N. A. Fleck, Frictionless indentation of dissimilar elastic-plastic spheres, Int. J. Solids Struct. 37 (46) (2000) 7071–7091. doi:https://doi.org/10.1016/S0020-7683(99)00328-5.

[134] S. D. Mesarovic, K. L. Johnson, Adhesive contact of elastic-plastic spheres, J. Mech. Phys. Solids 48 (10) (2000) 2009–2033. doi:https://doi.org/10.1016/S0022-5096(00)00004-1.

[135] J. Q. Feng, Adhesive Contact of Elastically Deformable Spheres: A Computational Study of Pull-Off Force and Contact Radius, J. Colloid Interface Sci. 238 (2) (2001) 318–323. doi:https://doi.org/10.1006/jcis.2001.7532.

[136] L. Kogut, I. Etsion, Adhesion in elastic-plastic spherical microcontact, J. Colloid Interface Sci. 261 (2) (2003) 372–378. doi:https://doi.org/10.1016/S0021-9797(03)00071-7.

[137] D. Maugis, H. M. Pollock, Surface forces, deformation and adherence at metal microcontacts, Acta Metallurgica 32 (9) (1984) 1323–1334. doi:https://doi.org/10.1016/0001-6160(84)90078-6.

[138] K. L. Johnson, Contact Mechanics, Cambridge University Press, 1985. doi:https://doi.org/10.1017/CBO9781139171731.

[139] D. Tabor, Surface forces and surface interactions, J. Colloid Inteface. Sci. 58 (1) (1977) 2–13. doi:https://doi.org/10.1016/0021-9797(77)90366-6.

[140] B. V. Derjaguin, V. M. Muller, Y. P. Toporov, Effect of contact deformations on the adhesion of particles, J. Colloid Interface Sci. 53 (2) (1975) 314–326. doi:https://doi.org/10.1016/0021-9797(75)90018-1.

[141] K. L. Johnson, K. Kendall, A. D. Roberts, Surface energy and the contact of elastic solids, Proc. R. Soc. Lond. A 324 (1558) (1971) 301–313. doi:https://doi.org/10.1098/rspa.1971.0141.

[142] M. Barquins, D. Maugis, Adhesive contact of axissymmetrical punches on an elastic half-space: the modified Hertz-Huber's stress tensor for concontacting spheres, J. Mechanique Theroique et Appliquee 1 (1982) 331–357.

[143] J. A. Greenwood, K. L. Johnson, An alternative to the Maugis model of adhesion between elastic spheres, J. Phys. D 31 (22) (1998) 3279–3290. doi:https://doi.org/10.1088/0022-3727/31/22/017.

[144] H. Rumpf, Grundlagen und methoden des granulierens, Chem. Ing. Tech. CIT 30 (3) (1958) 144–158. doi:https://doi.org/10.1002/cite.330300307.

[145] M. Suzuki, Packing Properties, in: Masuda, K. Higashitani, H. Yoshida (Eds.), Powder Technol. Fundam. Part. Powder Beds, Part. Gener., CRC Press, 2006, pp. 293–308.

[146] M. Nakagaki, H. Sunada, Theoretical studies on structures of the sedimentation bed of spherical particles, Yakugaku Zasshi 88 (6) (1968) 651–655.

[147] W. Zhang, Q. Sun, S. Zhu, B. Wang, Experimental study on mechanical and porous characteristics of limestone affected

by high temperature, Appl. Therm. Eng. 110 (2017) 356–362. doi:https://doi.org/10.1016/j.applthermaleng.2016.08.194.

[148] I. M. Daniel, Composite Materials: Testing and Design, 6th Conference/Stp 787, ASTM, 1982.

[149] R. Gunda, A. A. Volinsky, Tip-induced calcite single crystal nanowear, Mater. Res. Soc. Symp. Proc. 1049 (2007) 1049–AA05–15. doi:https://doi.org/10.1557/PROC-1049-AA05-15.

[150] N. S. Gupta, Chitin: Formation and Diagenesis, Topics in Geobiology, Springer Netherlands, 2010.

[151] A. Ghadami, J. Ghadam, Investigation of Mechanical Properties Prediction of Synthesized Nylon-66/Nano-Calcium Carbonate Composites, J. Part. Sci. Technol. 1 (4) (2015) 241–251. doi:http://dx.doi.org/10.22104/jpst.2015.307.

[152] S.-W. Lee, Y.-J. Kim, Y.-H. Lee, H. Guim, S. M. Han, Behavior and characteristics of amorphous calcium carbonate and calcite using CaCO3 film synthesis, Mater. Des. 112 (2016) 367–373. doi:https://doi.org/10.1016/j.matdes.2016.09.099.

[153] F. Pacheco-Torgal, C. Shi, A. Palomo, Carbon Dioxide Sequestration in Cementitious Construction Materials, Woodhead Publishing Series in Civil and Structural Engineering, Elsevier Science, 2018.

[154] [link].

URL https://www.crystran.co.uk/optical-materials/calcite-caco3

[155] [link].

URL https://www.surfacenet.de/calcite-217.html

[156] [link].

URL https://www.hubermaterials.com

[157] [link].

URL http://www.matweb.com

[158] G. Lomboy, S. Sundararajan, K. Wang, S. Subramaniam, A test method for determining adhesion forces and Hamaker constants of cementitious materials using atomic force microscopy, Cem. Concr. Res. 41 (11) (2011) 1157–1166. doi:https://doi.org/10.1016/j.cemconres.2011.07.004.

[159] S. K. Upadhyay, Seismic Reflection Processing: With Special Reference to Anisotropy, Springer, Berlin, Heidelberg, 2013.

[160] [link].

URL https://materialsproject.org/materials/mp-3953/

[161] A. T. Santhanam, Y. P. Gupta, Cleavage surface energy of calcite, Int. J. Rock Mech. Min. Sci. 5 (3) (1968) 253–259. doi:https://doi.org/10.1016/0148-9062(68)90013-2.

[162] A. Royne, J. Bisschop, D. K. Dysthe, Experimental investigation of surface energy and subcritical crack growth in calcite, J. Geophys. Res. 116 (B04204) (2011) 1–10. doi:https://doi.org/10.1029/2010JB008033.

Table 1: Mechanical properties reported in the literature for $CaCO_3$ at room temperature.

Young's Modulus E (GPa)	Mechanical Hardness H (GPa)	Poisson ratio ν (−)	Surface energy γ (J/m^2)
$25 - 88.19$[a]	$0.75 - 5.11$[b]	$0.21 - 0.34$[c]	$0.32 - 0.347$[d]

References: a [148–155], b [149, 152, 153, 156, 157], c [148–151, 158–160], and d [161, 162].

Table 2: Best fitting parameters (S. I. units) of the equation $\sigma_{\mathrm{t}} = a\sigma_{\mathrm{c}}^{\mathrm{b}}$ to experimental data (Figure 8). The fitting correlation factor is ρ^2.

$T(^{\circ}\mathrm{C})$	$d_{\mathrm{p}} = 32 \pm 1\,\mu\mathrm{m}$			$d_{\mathrm{p}} = 42.5 \pm 0.8\,\mu\mathrm{m}$		
	a	b	ρ^2	a	b	ρ^2
25	11 ± 1	0.25 ± 0.01	0.99065	3.6 ± 0.6	0.36 ± 0.03	0.98576
100	7 ± 1	0.39 ± 0.02	0.98814	6 ± 3	0.37 ± 0.07	0.90005
200	6 ± 3	0.46 ± 0.08	0.92055	3.1 ± 0.7	0.54 ± 0.03	0.9903
300	3.2 ± 0.9	0.62 ± 0.04	0.98669	2.05 ± 0.8	0.67 ± 0.06	0.9792
400	0.3 ± 0.2	1.0 ± 0.1	0.96783	1.6 ± 0.4	0.80 ± 0.03	0.99333
500	0.2 ± 0.1	1.16 ± 0.1	0.98597	2 ± 1	0.8 ± 0.1	0.95804
$T(^{\circ}\mathrm{C})$	$d_{\mathrm{p}} = 59.3 \pm 0.8\,\mu\mathrm{m}$			$d_{\mathrm{p}} = 88.2 \pm 0.7\,\mu\mathrm{m}$		
	a	b	ρ^2	a	b	ρ^2
25	1.8 ± 0.3	0.43 ± 0.03	0.98922	1.9 ± 0.6	0.39 ± 0.05	0.95489
100	2.7 ± 0.7	0.44 ± 0.04	0.97969	5 ± 1	0.31 ± 0.03	0.9755
200	9 ± 2	0.35 ± 0.03	0.97956	7 ± 1	0.33 ± 0.03	0.97772
300	2.8 ± 0.6	0.59 ± 0.03	0.99163	1.2 ± 0.4	0.67 ± 0.05	0.98112
400	1.4 ± 0.5	0.79 ± 0.05	0.98719	3 ± 2	0.67 ± 0.08	0.9562
500	1.3 ± 0.4	0.84 ± 0.04	0.99335	1.2 ± 0.4	0.85 ± 0.05	0.99127

Table 3: Best fitting parameters (S. I. units) of the equation $\phi = c + d\ln\sigma_{\mathrm{c}}$ to data in Figure 12. The fitting correlation factor is ρ^2.

	$d_{\mathrm{p}} = 32 \pm 1\,\mu\mathrm{m}$			$d_{\mathrm{p}} = 42.5 \pm 0.8\,\mu\mathrm{m}$		
$T(^\circ\mathrm{C})$	c	d	ρ^2	c	d	ρ^2
25	0.377 ± 0.008	0.014 ± 0.001	0.981762	0.42 ± 0.01	0.010 ± 0.002	0.911592
100	0.33 ± 0.01	0.019 ± 0.002	0.974538	0.383 ± 0.005	0.0114 ± 0.0008	0.985863
200	0.27 ± 0.02	0.025 ± 0.002	0.97092	0.33 ± 0.01	$0.017 \pm 0.0.002$	0.975466
300	0.23 ± 0.03	0.028 ± 0.005	0.927938	0.26 ± 0.02	$0.025 \pm 0.0.002$	0.974871
400	0.04 ± 0.05	0.051 ± 0.007	0.940588	0.21 ± 0.02	0.029 ± 0.003	0.968876
500	-0.4 ± 0.1	0.10 ± 0.02	0.871666	0.11 ± 0.06	0.038 ± 0.008	0.876716

	$d_{\mathrm{p}} = 59.3 \pm 0.8\,\mu\mathrm{m}$			$d_{\mathrm{p}} = 88.2 \pm 0.7\,\mu\mathrm{m}$		
$T(^\circ\mathrm{C})$	c	d	ρ^2	c	d	ρ^2
25	0.446 ± 0.006	0.0080 ± 0.0009	0.96668	0.511 ± 0.002	0.0025 ± 0.0003	0.95278
100	0.435 ± 0.007	0.006 ± 0.001	0.92688	0.477 ± 0.007	0.005 ± 0.001	0.889436
200	0.353 ± 0.003	0.0149 ± 0.0004	0.997859	0.452 ± 0.007	$0.008 \pm 0.0.0001$	0.961141
300	0.30 ± 0.01	0.020 ± 0.002	0.981252	0.434 ± 0.009	0.009 ± 0.001	0.957253
400	0.27 ± 0.02	0.023 ± 0.003	0.954567	0.418 ± 0.009	$0.0.010 \pm 0.001$	0.953974
500	0.19 ± 0.01	0.032 ± 0.002	0.986809	0.38 ± 0.02	0.013 ± 0.004	0.82149

Table 4: Slope $m_{\text{exp}} = F_{\text{t}}/\sqrt{F_{\text{c}}}$ of the best linear fitting of estimated data of the pull-off force and the square root of the compressive force from experimental measurements of the bulk tensile yield strength and consolidation stress, respectively (Figure 13). The fitting correlation factor is ρ^2.

$T(°\text{C})$	m_{exp} $(\sqrt{nN})$	ρ^2
25	2.4 ± 0.2	0.933621
100	3.9 ± 0.3	0.921107
200	5.6 ± 0.3	0.93635
300	15.5 ± 0.5	0.983518
400	37.8 ± 0.9	0.988935
500	69 ± 3	0.968318
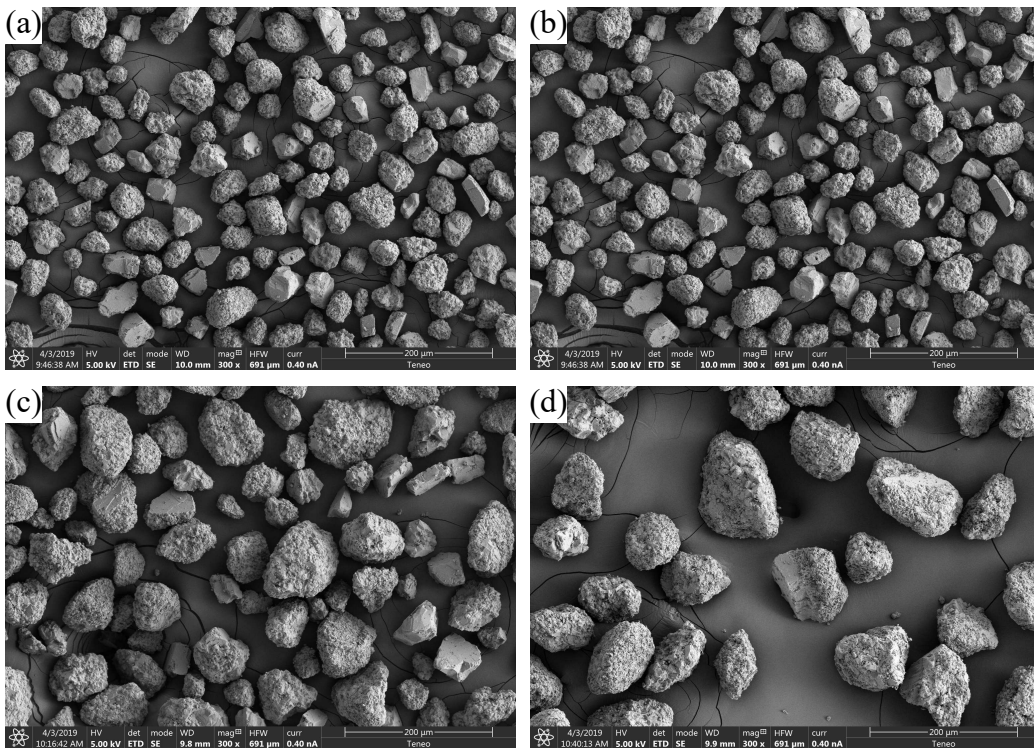
Figure 1: Scanning electron microscopy (SEM) pics of the tested $CaCO_3$ particles with an average particle size of (a) $d_p = 32 \pm 1\,\mu m$ –Eskal30–; (b) $d_p = 42.5 \pm 0.8\,\mu m$ –Eskal45–; (c) $d_p = 59.3 \pm 0.8\,\mu m$ –Eskal60–; and (d) $d_p = 88.2 \pm 0.7\,\mu m$ –Eskal80– as measured from laser diffractometry (Figure 2).
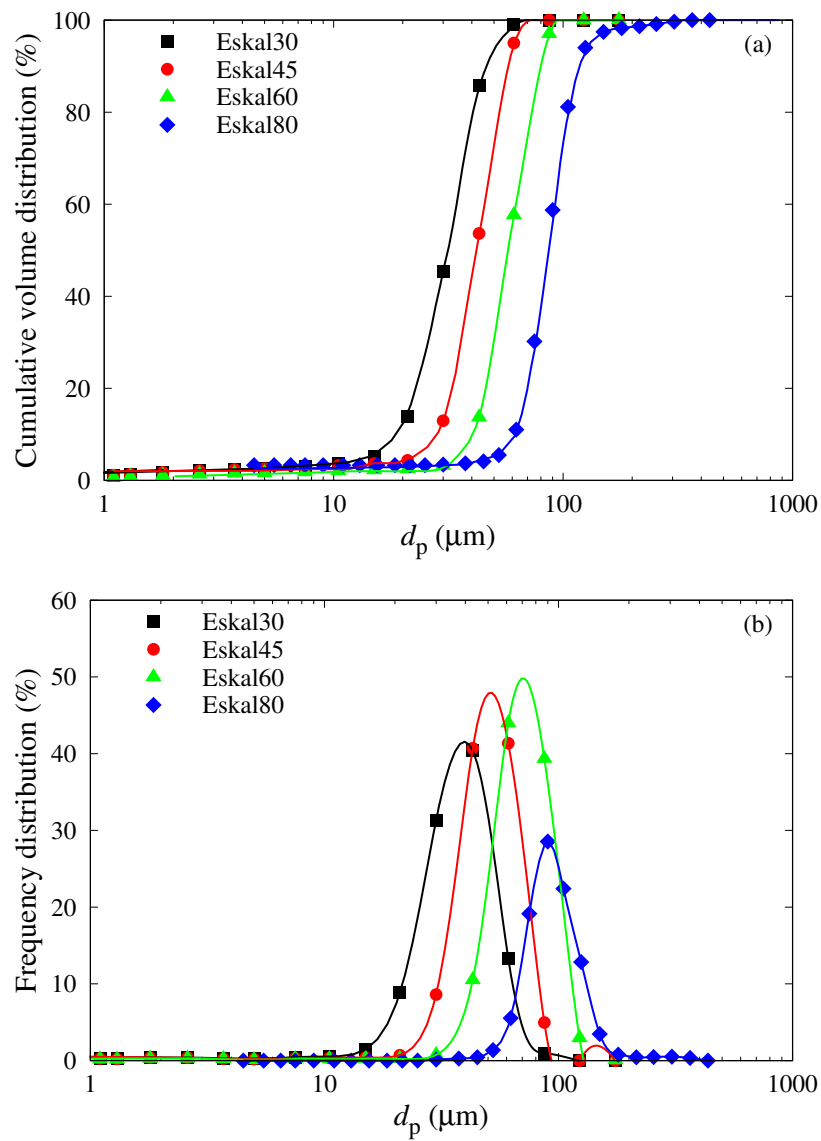
Figure 2: Cumulative volume distribution (a) and number distribution (b) of particle sizes d_p for the tested $CaCO_3$ powders. Lines between dots are a guide to the eye.
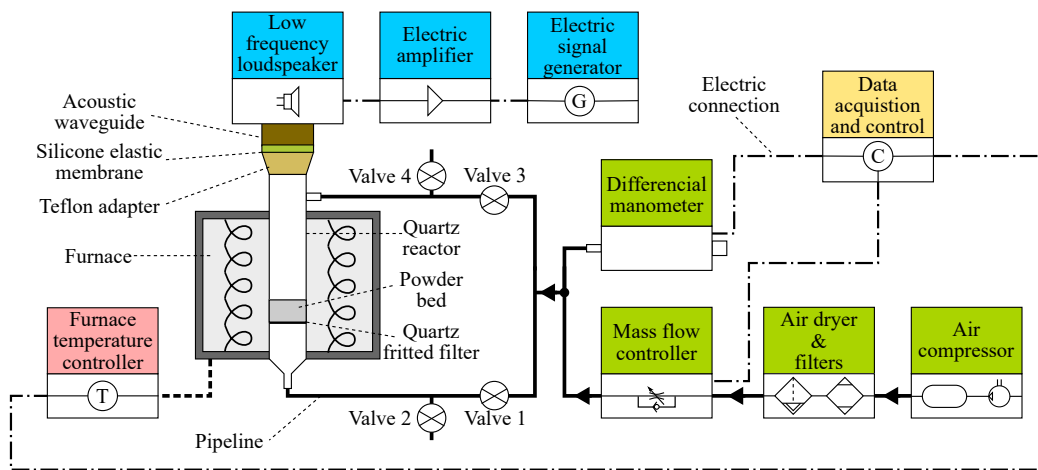
Figure 3: Sketch of the experimental set-up used in the experiments reported in this paper.
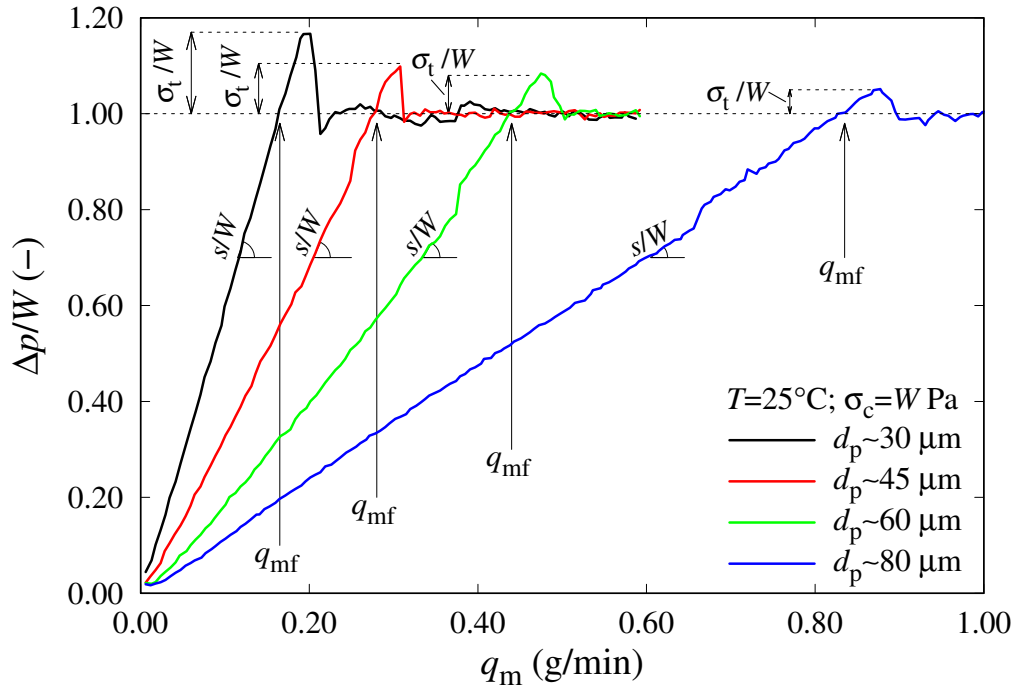
Figure 4: Experimental curves of the gas pressure drop across the powder bed Δp (normalized by the powder's weight per unit area W) as a function of the gas flow rate q_m for samples of $CaCO_3$ powders of different particle size d_p (indicated). The vertical lines indicate the minimum fluidization gas flow rate q_{mf}; the tensile yield strength of the bed σ_t; and the initial slope s between Δp and q_m (before fracture of the bed). In these tests, samples were previously consolidated to $\sigma_c = W$ Pa at room temperature.
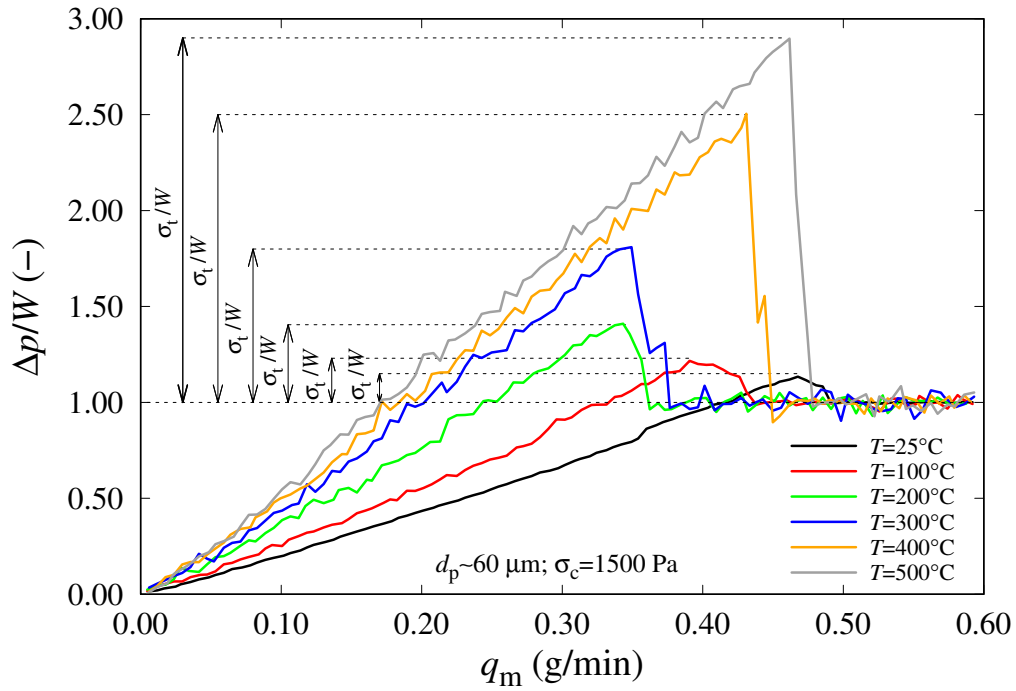
Figure 5: Examples of gas pressure drop curves across the $CaCO_3$ powder bed (made non dimensional with the powder's weight per unit area) $\Delta p/W$ versus the gas flow rate q_m for samples of average particle size $d_p = 59.3 \pm 0.8\,\mu m$ previously subjected to a consolidation stress of $\sigma_c = 1500\,Pa$. The inset shows the temperatures at which the experiments were performed. Vertical lines indicate the measured tensile yield strength for each temperature.
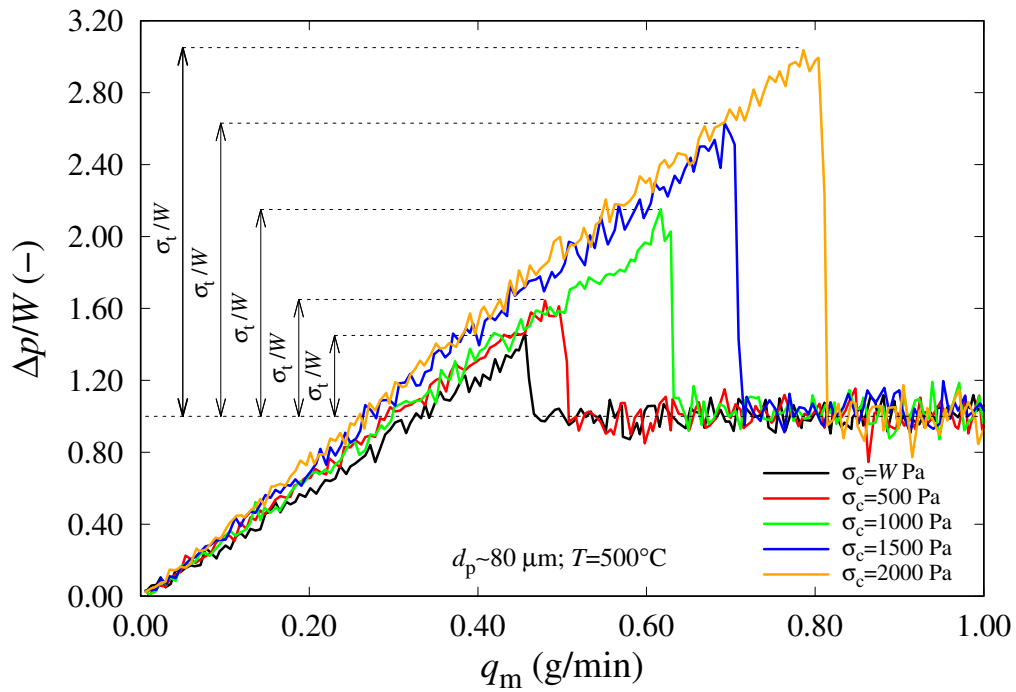
Figure 6: Normalized gas pressure drop across the powder bed $\Delta p/W$ as a function of the gas flow rate q_{m} for CaCO$_3$ samples of average particle size $d_{\mathrm{p}} = 88.02 \pm 0.7\,\mu\mathrm{m}$. These experiments were carried out at $T = 500°\mathrm{C}$ at different consolidation stresses σ_{c} as indicated which were applied to the beds previously to breaking.
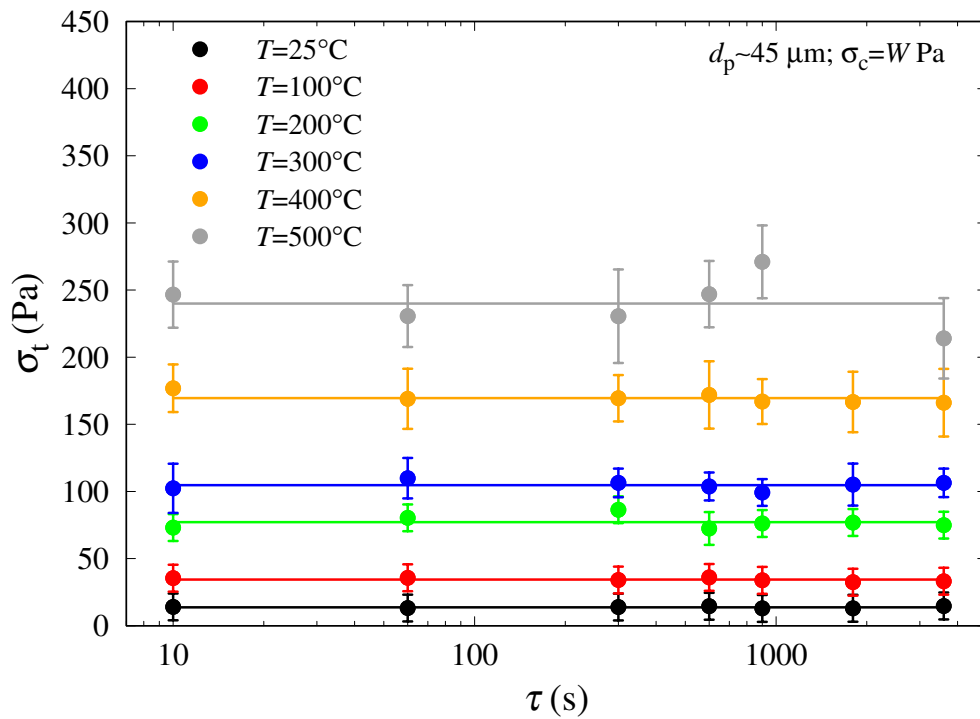
Figure 7: Measured tensile yield strength σ_t as a function of the period of time τ during the powder bed was subjected to a consolidation stress $\sigma_c = W$ Pa before breaking for the indicated temperatures. The solid lines represent average values of the experimental data. Particle size of the tested sample was $d_p = 42.5 \pm 0.8\,\mu$m.
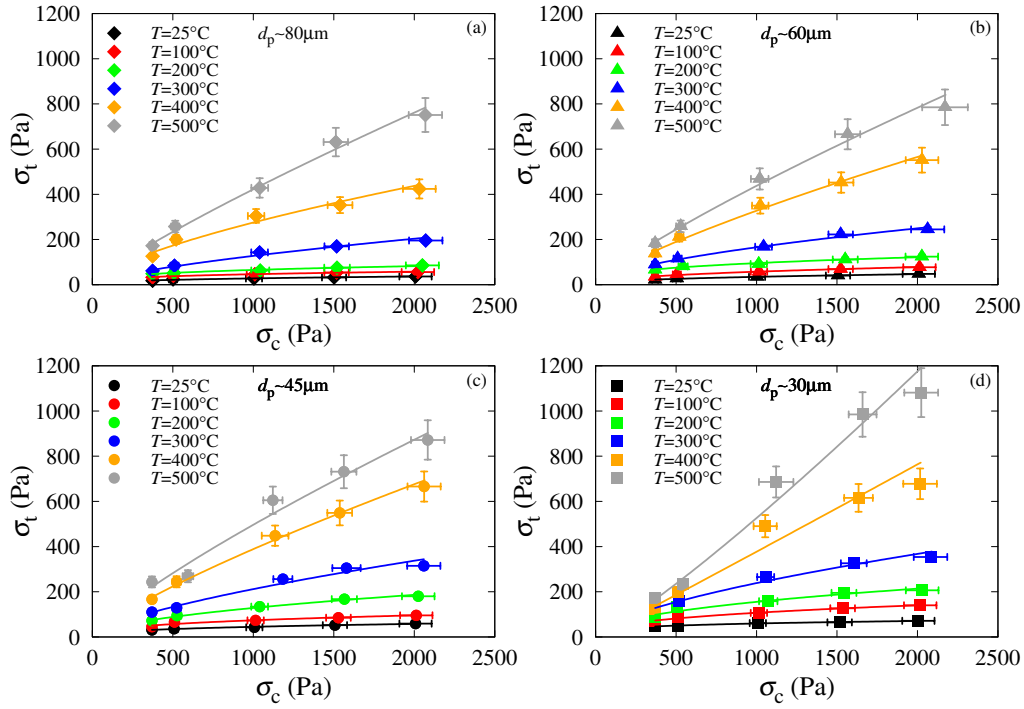
Figure 8: Tensile yield strength of the powder bed σ_t as a function of the previously applied consolidation stress σ_c and temperature T for $CaCO_3$ samples of different particle size: (a) $d_p = 88.2 \pm 0.7\,\mu$m; (b) $d_p = 59.3 \pm 0.8\,\mu$m; (c) $d_p = 42.5 \pm 0.8\,\mu$m; and (d) $d_p = 32 \pm 1\,\mu$m. The solid lines represent the best fittings of the equation $\sigma_t = a\sigma_c^b$ to the experimental data. Best fitting parameters are reported in Table 2.
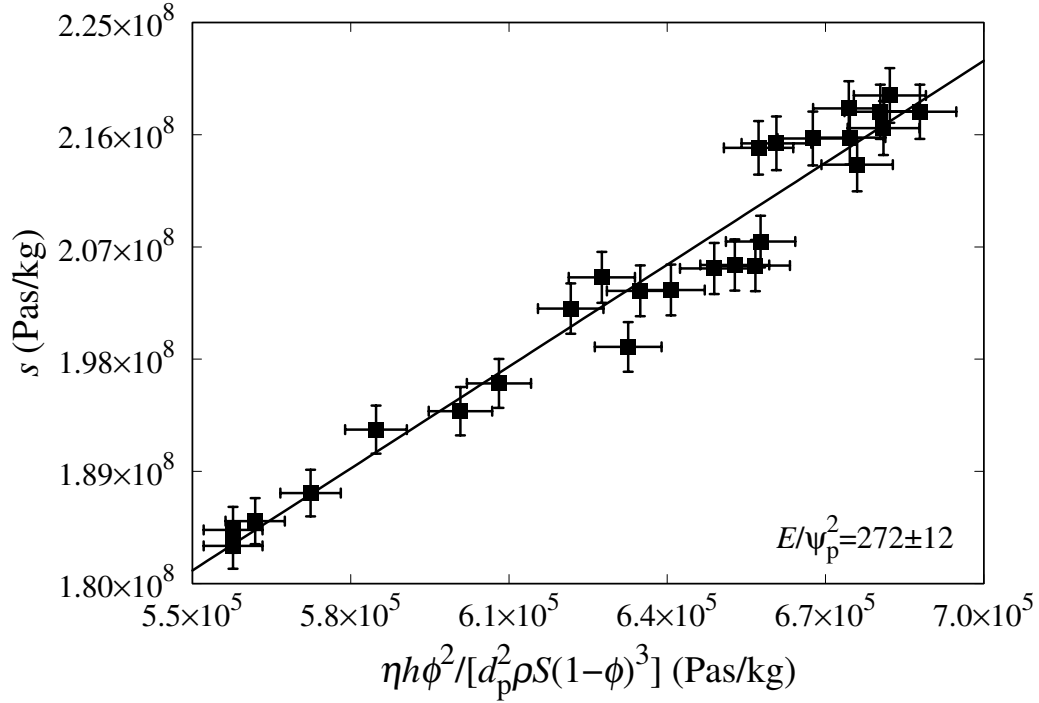
Figure 9: Measured slope s of the gas pressure drop Δp vs. the gas flow rate q_m (before the breakup of the bed) as a function of $\eta h\phi^2/[\rho S d_\mathrm{p}^2(1-\phi)^3]$, where h is the measured height of the powder bed previously subjected to a consolidation stress σ_c; S is the cross sectional area of the powder bed; η and ρ are the air viscosity and density ($T = 25^\circ$C for these data), respectively; and ϕ denotes the particle volume fraction calculated as $\phi = m_\mathrm{p}/(\rho_\mathrm{p} S h)$ (being m_p the mass of powder and ρ_p the density of the material). According to the Carman-Kozeny law (Equation 2), the slope of the best linear fitting corresponds to the ratio of the Ergun constant to the square of the sphericity of the particles E/ψ_p^2 (indicated).
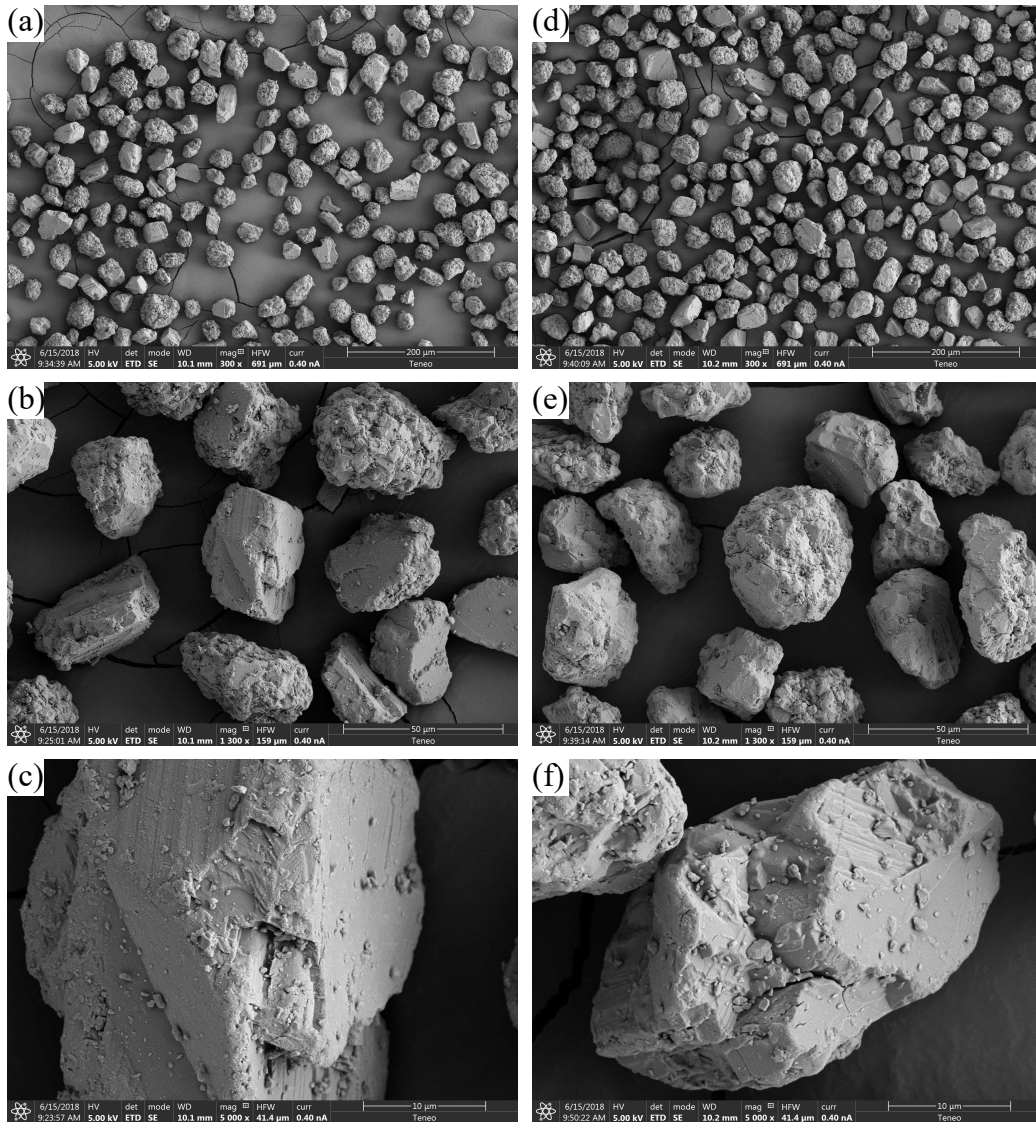
Figure 10: SEM images of CaCO$_3$ particles of average size $d_{\mathrm{p}} = 32 \pm 1\,\mu$m at room temperature (a-b-c) and after heating them up to $T = 500°$C (d-e-f).
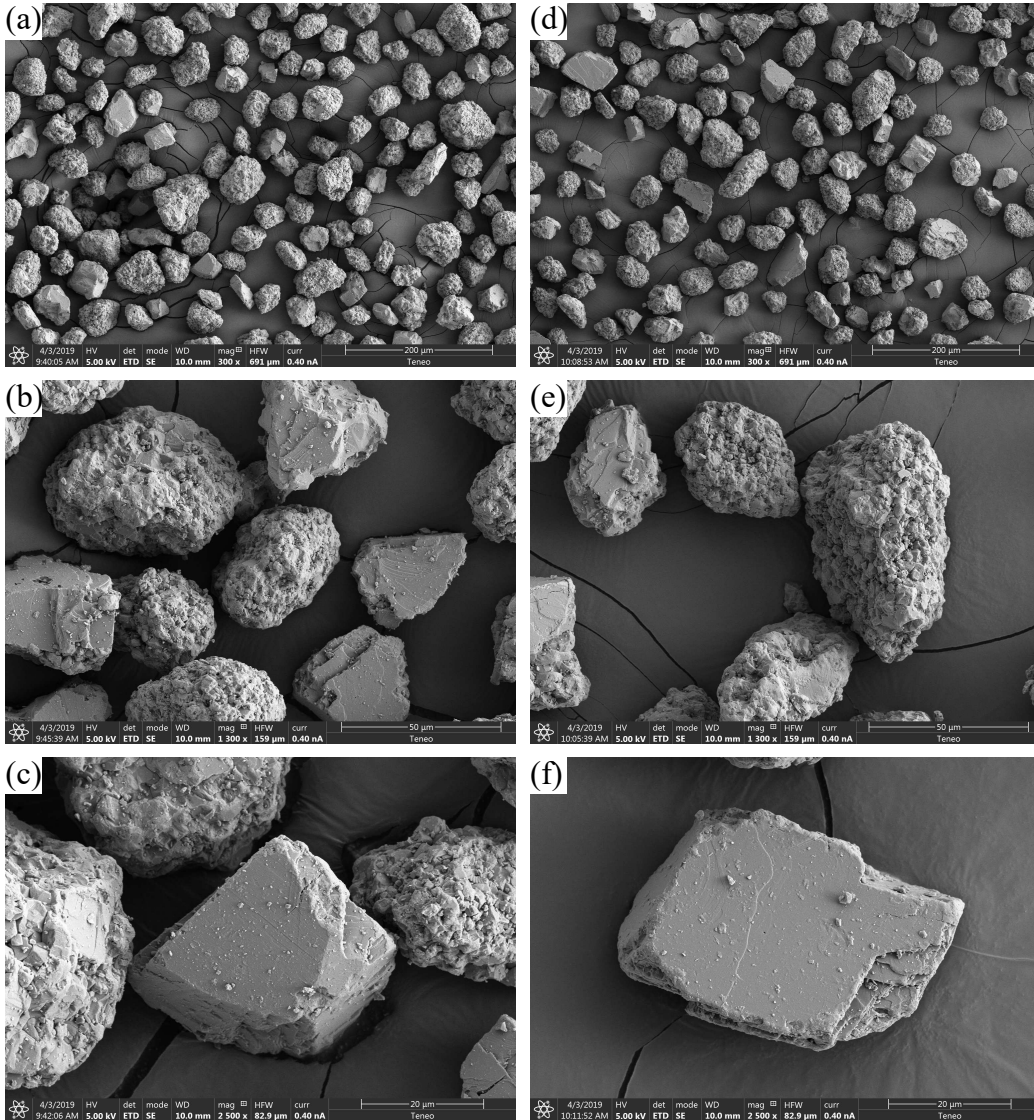
Figure 11: SEM images of CaCO$_3$ particles of average size $d_{\mathrm{p}} = 42.5 \pm 0.8\,\mu$m at room temperature (a-b-c) and after heating them up to $T = 500°$C (d-e-f).
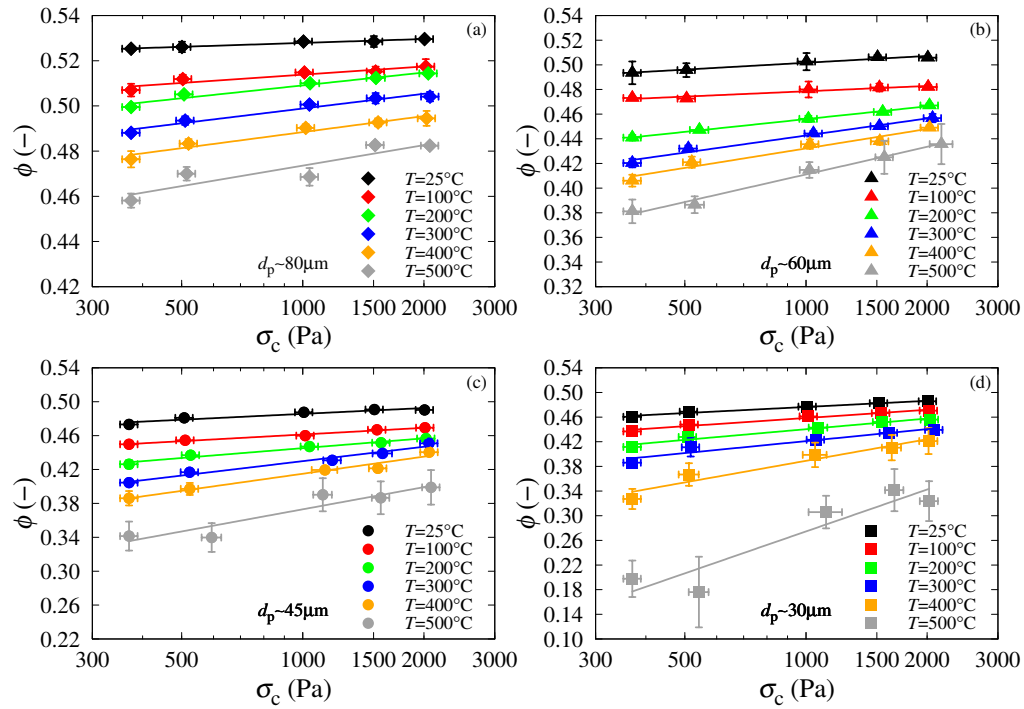
Figure 12: Particle volume fraction before the fracture of the bed ϕ as a function of the previously imposed consolidation stress σ_c for $CaCO_3$ powders of different particle size: (a) $d_p = 88.2 \pm 0.7\,\mu m$; (b) $d_p = 59.3 \pm 0.8\,\mu m$; (c) $d_p = 42.5 \pm 0.8\,\mu m$; and (d) $d_p = 32 \pm 1\,\mu m$. The lines correspond to the best fittings of the equation $\phi = c + d \ln \sigma_c$ to the experimental data. Best fitting parameters are reported in Table 3.
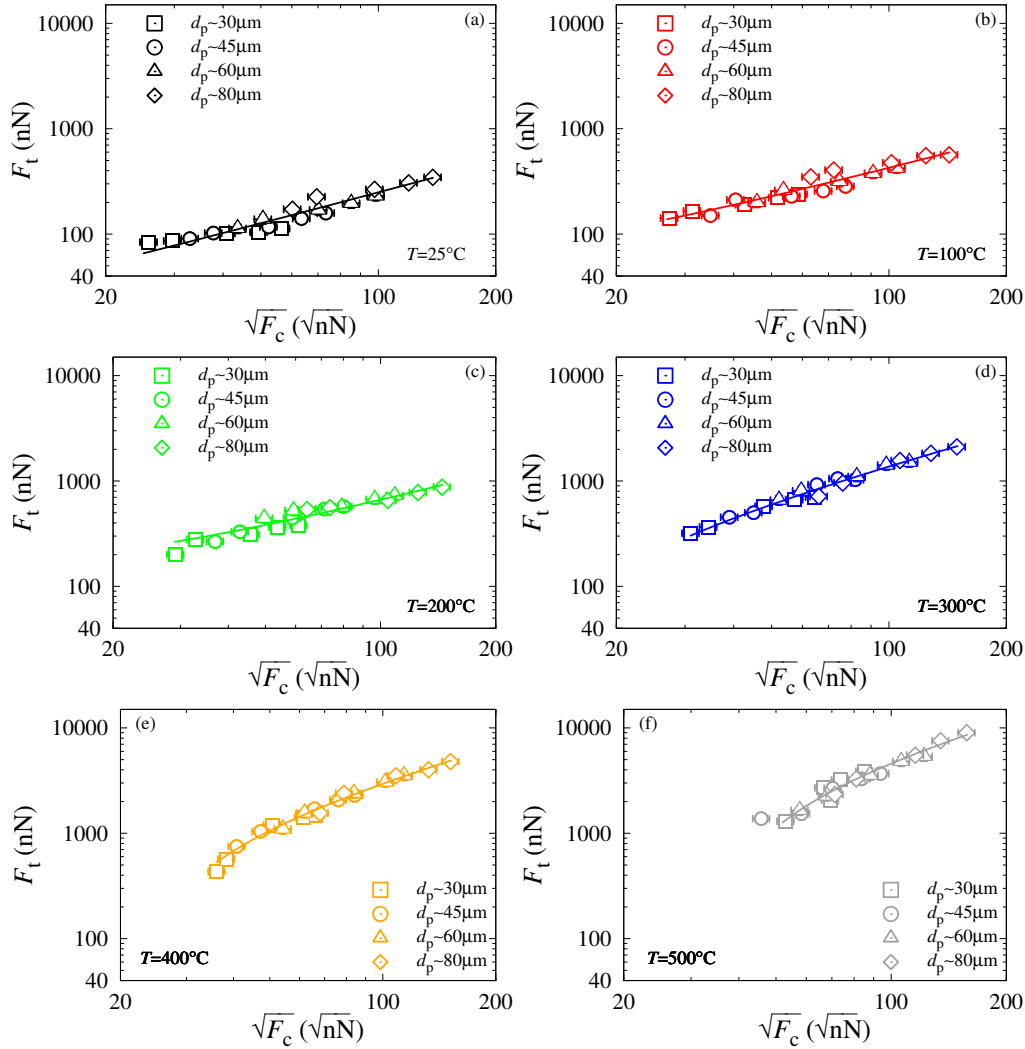
Figure 13: Log-log plot of the calculated interparticle pull-off force F_t as a function of the square root of the compressive force per contact F_c for $CaCO_3$ powder samples of different particle size and at different temperatures: (a) $T = 25°C$; (b) $T = 100°C$; (c) $T = 200°C$; (d) $T = 300°C$; (e) $T = 400°C$; and (f) $T = 500°C$. The solid lines correspond to the linear fittings of the experimental data. Best fitting slopes $m_{exp} = F_t/\sqrt{F_c}$ are reported in Table 4.